QSR

The middle Pleistocene transition: characteristics, mechanisms, and implications for long-term changes in atmospheric pCO$_2$

Peter U. Clark[a],*, David Archer[b],**, David Pollard[c], Joel D. Blum[d], Jose A. Rial[e], Victor Brovkin[f], Alan C. Mix[g], Nicklas G. Pisias[g], Martin Roy[h]

[a]*Department of Geosciences, Oregon State University, Corvallis, OR 97331, USA*
[b]*Department of Geophysical Sciences, University of Chicago, Chicago, IL 60637, USA*
[c]*Earth System Science Center, Pennsylvania State University, University Park, PA 16802, USA*
[d]*Department of Geological Sciences, University of Michigan, Ann Arbor, MI 48109, USA*
[e]*Wave Propagation Laboratory, Department of Geological Sciences, University of North Carolina, Chapel Hill, NC 27599, USA*
[f]*Potsdam Institute for Climate Impact Research, Climate Systems Research Department, 14412 Potsdam, Germany*
[g]*College of Oceanic and Atmospheric Sciences, Oregon State University, Corvallis, OR 97331, USA*
[h]*Département des Sciences de la Terre et de l'Atmosphère, Université du Québec à Montréal, Montréal, QC H3C 3P8, Canada*

Abstract

The emergence of low-frequency, high-amplitude, quasi-periodic (∼100-kyr) glacial variability during the middle Pleistocene in the absence of any significant change in orbital forcing indicates a fundamental change internal to the climate system. This middle Pleistocene transition (MPT) began 1250 ka and was complete by 700 ka. Its onset was accompanied by decreases in sea surface temperatures (SSTs) in the North Atlantic and tropical-ocean upwelling regions and by an increase in African and Asian aridity and monsoonal intensity. During the MPT, long-term average ice volume gradually increased by ∼50 m sea-level equivalent, whereas low-frequency ice-volume variability experienced a 100-kyr lull centered on 1000 ka followed by its reappearance ∼900 ka, although as a broad band of power rather than a narrow, persistent 100-kyr cycle. Additional changes at 900 ka indicate this to be an important time during the MPT, beginning with an 80-kyr event of extreme SST cooling followed by the partial recovery and subsequent stabilization of long-term North Atlantic and tropical ocean SSTs, increasing Southern Ocean SST variability primarily associated with warmer interglacials, the loss of permanent subpolar sea-ice cover, and the emergence of low-frequency variability in Pacific SSTs and global deep-ocean circulation. Since 900 ka, ice sheets have been the only component of the climate system to exhibit consistent low-frequency variability. With the exception of a near-universal organization of low-frequency power associated with marine isotope stages 11 and 12, all other components show an inconsistent distribution of power in frequency-time space, suggesting a highly nonlinear system response to orbital and ice-sheet forcing.

Most hypotheses for the origin of the MPT invoke a response to a long-term cooling, possibly induced by decreasing atmospheric pCO$_2$. None of these hypotheses, however, accounts for the geological constraint that the earliest Northern Hemisphere ice sheets covered a similar or larger area than those that followed the MPT. Given that the MPT was associated with an increase in ice volume, this constraint requires that post-MPT ice sheets were substantially thicker than pre-MPT ice sheets, indicating a change in subglacial conditions that influence ice dynamics. We review evidence in support of the hypothesis that such an increase in ice thickness occurred as crystalline Precambrian Shield bedrock became exposed by glacial erosion of a thick mantle of regolith. This exposure of a high-friction substrate caused thicker ice sheets, with an attendant change in their response to the orbital forcing. Marine carbon isotope data indicate a rapid transfer of organic carbon to inorganic carbon in the ocean system during the MPT. If this carbon came from terrigenous sources, an increase in atmospheric pCO$_2$ would be likely, which is inconsistent with evidence for widespread cooling, Apparently rapid carbon transfer from terrestrial sources is difficult to reconcile with gradual erosion of regolith. A more likely source of organic carbon and nutrients (which would mitigate pCO$_2$ rise) is from shelf and upper slope marine sediments, which were fully exposed for the first time in millions of years in response to thickening ice sheets and falling sealevels during the MPT. Modeling indicates that regolith

---

*Corresponding author. Tel.: +1 541 737 1247; fax: +1 541 737 1200.
**Also to be corresponded to. Tel.: +1 773 702 0823.
E-mail addresses: clarkp@onid.orst.edu (P.U. Clark), d-archer@uchicago.edu (D. Archer).

erosion and resulting exposure of crystalline bedrock would cause an increase in long-term silicate weathering rates, in good agreement with marine Sr and Os isotopic records. We use a carbon cycle model to show that a post-MPT increase in silicate weathering rates would lower atmospheric pCO_2 by 7–12 ppm, suggesting that the attendant cooling may have been an important feedback in causing the MPT.

1. Introduction

N.J. Shackleton's fundamental contributions to our understanding of climate variability at orbital timescales (10^4–10^5 yr) continue to define the field today. Hays et al. (1976) first established that the timing of variations in the Earth's orbit around the Sun corresponded to variations in Earth's climate over the last 430,000 years, providing strong support for the Milankovitch hypothesis for the cause of the ice ages. They also concluded that while climate responded linearly to precession (23 kyr) and obliquity (41 kyr), the dominant response over this interval has been to the small eccentricity forcing at 100 kyr, requiring some nonlinear amplification of the forcing.

Concurrently, Shackleton and Opdyke (1976) published a detailed benthic $\delta^{18}O$ ($\delta^{18}O_b$) record from marine core V28-239 in the equatorial Pacific Ocean that, for the first time, extended the record of orbital-scale variability beyond the Brunhes/Matuyama magnetic reversal, spanning the entire Pleistocene and extending into the late Pliocene (Fig. 1a). This record was surprising, however, in revealing that the dominant high-amplitude 100-kyr climate cycle only emerged sometime during late Matuyama time; prior to that, climate varied at lower amplitude 41-kyr cycles (Fig. 1a). Using time-series analytical methods, Pisias and Moore (1981) confirmed the spectral change seen in V28-239, which has since become generally known as the middle Pleistocene transition (MPT). Moreover, they noted that because variations in the Earth's orbital parameters did not change over the last 2000 ka, "the nature of the climate response, as well as its time constant to external forcing, may have evolved and changed with time" (p. 451). Accordingly, Shackleton helped establish two interrelated questions that remain at the forefront of paleoclimate research: the emergence of the 100-kyr climate cycle in the absence of any change in the
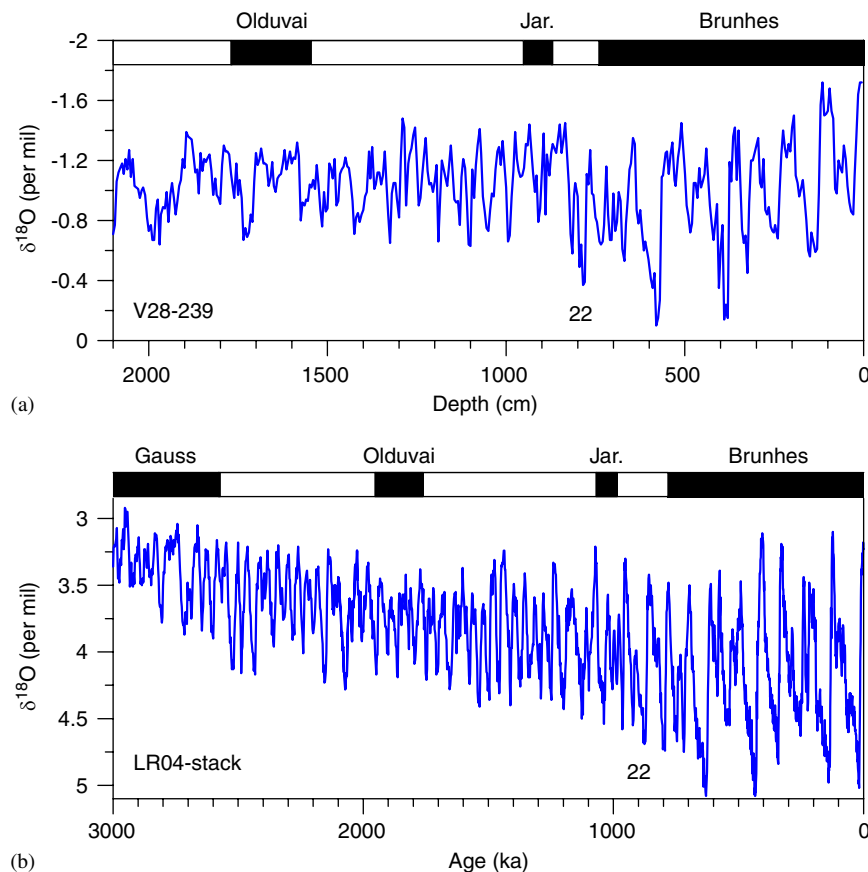

Fig. 1. (a) The $\delta^{18}O_b$ record from marine core V28-239, plotted on its depth scale, with corresponding paleomagnetic intervals (Shackleton and Opdyke, 1976), (b) The LR04 $\delta^{18}O_b$ stack for the last 3 Myr, representing 57 globally distributed sites (Lisiecki and Raymo, 2005). The location of marine isotope stage 22 is shown in both records for a common point of reference.

orbital forcing, and its subsequent dominance of orbital-scale climate variability when known forcing at that frequency (eccentricity) is the weakest of the three orbital variations.

In this paper, we further describe the characteristics of the MPT with regard to the onset of high-amplitude 100-kyr climate cycles in marine records of $\delta^{18}O$, which is the hallmark of the MPT as first defined in the V28-239 record (Shackleton and Opdyke, 1976) (Fig. 1a). We then address the question of how much of the increased amplitude of $\delta^{18}O_b$ variability during the MPT represents increased ice volume relative to decreased deep-water temperature. We next examine other climate records spanning much or all of the last 2500 kyr in order to evaluate the expression of the MPT in other components of the climate system. After summarizing previous hypotheses for the origin of the MPT, we discuss further the hypothesis proposed by Clark and Pollard (1998) that erosion of a regolith layer and subsequent exposure of Precambrian crystalline shield bedrock led to a change in ice-sheet response to orbital forcing that gave rise to the MPT. Based on this hypothesis, we then present modeling results that simulate the effect of exposure of fresh silicate bedrock on glacial–interglacial and long-term weathering rates. Lastly, we use a carbon cycle model that determines how simulated changes in weathering rates would affect atmospheric pCO_2.

2. When did the MPT occur?

Although the 41-kyr world of the late Pliocene/early Pleistocene is readily distinguishable from the 100-kyr world of the late Pleistocene (Fig. 1), there is wide disagreement in defining when the MPT occurred, with descriptions ranging from an abrupt versus gradual transition that began as early as 1500 ka and as late as 600 ka (e.g., Pisias and Moore, 1981; Prell, 1982; Ruddiman et al., 1989; Park and Maasch, 1993; Mudelsee and Schulz, 1997; Rutherford and D'Hondt, 2000). To some extent, these differing conclusions may be semantic in terms of how the MPT is defined, but we attribute much of this disagreement to the use of differing $\delta^{18}O$ records. At any particular site, the $\delta^{18}O$ signal may include local-to-regional changes in temperature or (particularly for planktic records) salinity, thus obscuring global changes in ice volume and deep-water temperature associated with the MPT. In addition, individual $\delta^{18}O$ records may have differing age models, which may result not only in differing estimates for the age of the MPT, but for characterizing how quickly it occurred as well (Park and Maasch, 1993).

We are now in a better position to address the question of when the MPT occurred by examining the "stacked" $\delta^{18}O_b$ record that Lisiecki and Raymo (2005) constructed by averaging 57 globally distributed sites (referred to herein as the LR04 stack) (Fig. 1b). The advantage of this record is its high signal-to-noise ratio, thus removing regional

variability and better capturing the global climate signal in $\delta^{18}O_b$.

We examine the MPT in the LR04 stack on the basis of the MPT's two defining characteristics: the increase in amplitude and decrease in frequency of the marine $\delta^{18}O$ signal. In the next section, we discuss the question of a temperature versus ice volume control on the $\delta^{18}O_b$ signal, but the important observation for current purposes is that the increase in amplitude across the MPT is associated primarily with glaciations (Fig. 2a), which should then be accompanied by an increase in the mean $\delta^{18}O_b$ value. In the LR04 stack, the interval following the onset of Northern Hemisphere glaciation 2800 ka until 2400 ka is associated with an increase in mean $\delta^{18}O_b$ of 0.75 per mil Myr^{-1} (not shown), indicating a 400-kyr interval when some combination of increasing ice volume and decreasing deep-water temperature accompanied successive glaciations. After 2400 ka, mean $\delta^{18}O_b$ increased by only 0.23 per mil Myr^{-1} until 1250 ka, when mean $\delta^{18}O_b$ started to increase by 0.64 per mil Myr^{-1}. By 700 ka, mean $\delta^{18}O_b$ reached its maximum value, where it has remained largely unchanged to the present (Fig. 2b). As expected, the increased amplitude of glacial cycles beginning 1250 Ma is reflected by an increase in the standard deviation of the LR04 stack as well (Fig. 2c). We note that the "hump" in both the mean and standard deviation of the LR04 stack centered on 1500 Ma is associated with a change in the amplitude of the 41-kyr cycle.

We next examine the timing of the emergence of low-frequency variability in the LR04 stack. In the LR04 record, the low-frequency (~100-kyr) climate cycle emerged 1250 ka and reached its full amplitude by 700 ka (Fig. 2d–f). If anything, this may slightly overestimate the duration of the transition, because the time window for spectral calculation is 350 kyr, and the spectral estimates constitute an average over this time window. Low-frequency power exhibits a ~100-kyr lull centered on 1000 ka (marine isotope stages 25–29), with renewed power beginning at ~900 ka (marine isotope stages 22 and 24) (Fig. 2e, f). Finally, the low-frequency $\delta^{18}O_b$ signal in the LR04 stack that emerged 1250 ka is characterized by a broad band of power rather than a narrow, persistent 100-kyr cycle (Fig. 2f), indicating an age and frequency-dependent response to low-frequency orbital forcing (e.g., Rial, 1999; Berger et al., 2005), a variable response to higher-frequency orbital forcing (e.g., Imbrie and Imbrie, 1980; Raymo, 1997; Huybers and Wunsch, 2005), or a variable timescale of an internal climate oscillation (e.g., Saltzman, 1982; Marshall and Clark, 2002). Only over the last 700 kyr has this signal exhibited its strongest power in frequency-time space with a quasi-periodicity of ~100 kyr.

Overall, these results thus suggest that the MPT was characterized by an increase in the severity of glaciations that paralleled the emergence of the ~100-kyr cycle starting at 1250 ka, with maximum glaciations being established at the same time (700 ka) as the establishment of the dominant 100-kyr cycles.
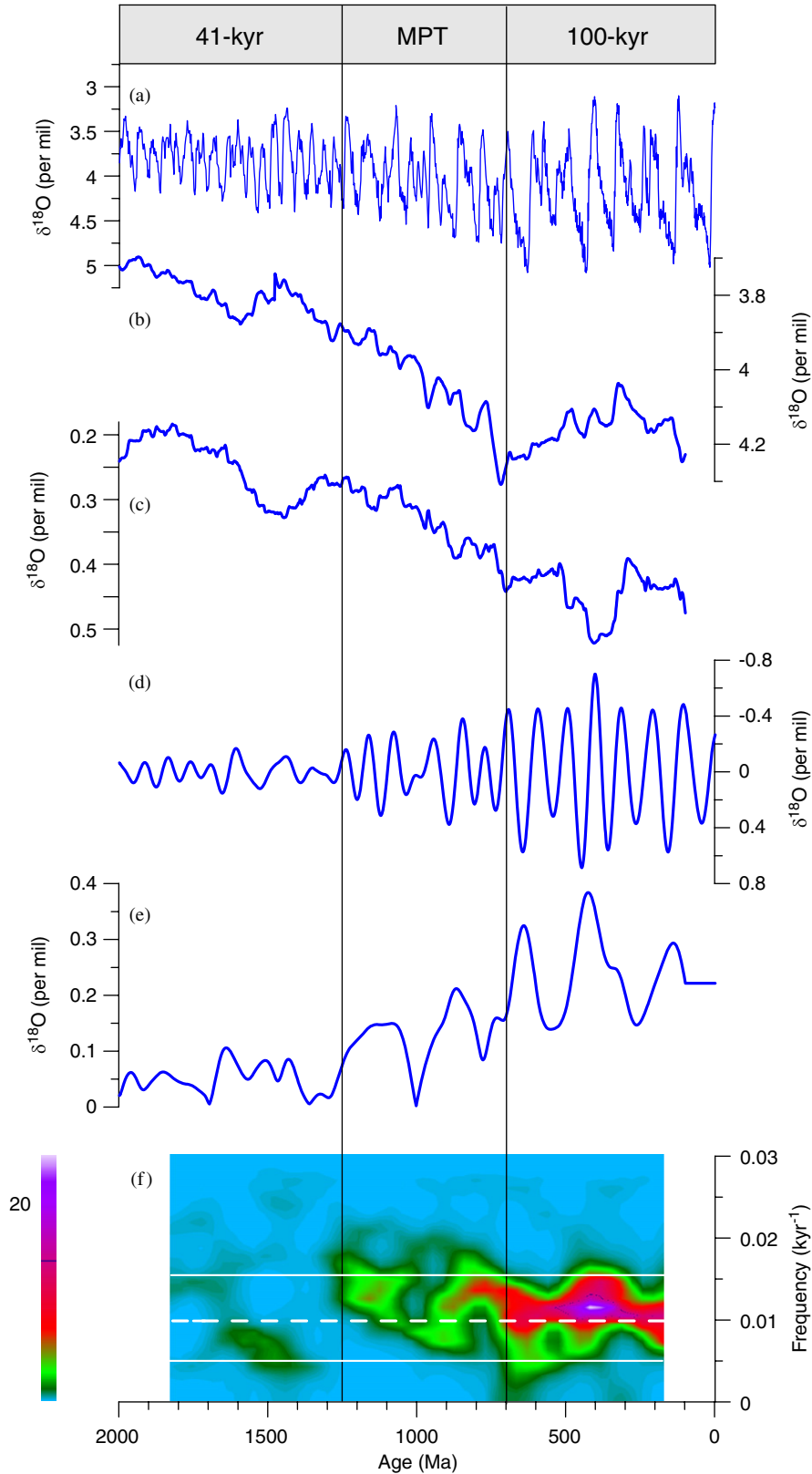
Fig. 2. (a) The LR04 $\delta^{18}O_b$ stack (Lisiecki and Raymo, 2005), (b) The mean of the LR04 stack, calculated using a 200-kyr sliding window, (c) The standard deviation of the LR04 stack, calculated using a 200-kyr sliding window, (d) Filtered LR04 stack using a 100-kyr filter, (e) Amplitude of the 100-kyr component of the LR04 stack as determined by complex demodulation, (f) Time-frequency spectrogram (moving window Fourier transform) showing the distribution of low-frequency power in the 100-kyr filtered LR04 $\delta^{18}O_b$ stack (cycles/kyr) (window length 350 kyr, sliding window length 35 kyr, high-pass filter = 0.00125, low-pass filter = 0.025). Broad light-gray vertical bar shows timing of the MPT as suggested by these indices.

3. Benthic $\delta^{18}O$, sea level, and ice volume changes during the MPT

For any given species of benthic foraminifera, variations in the $\delta^{18}O$ of its calcite test reflect some combination of local to regional changes in water mass properties (largely deep-water temperature) and global changes in seawater $\delta^{18}O$ ($\delta^{18}O_{SW}$) resulting from the growth and decay of land ice. Determining how much each of these components contributes to any given $\delta^{18}O_b$ record, however, remains ambiguous. In developing the first long Pleistocene $\delta^{18}O$ records, Emiliani (1955) interpreted the signal measured in planktonic records to be largely ($\sim 70\%$) temperature, with only a small fraction corresponding to changes in global ice volume. Subsequently, Shackleton (1967) argued that the reverse was true, with changes in $\delta^{18}O_b$ largely recording changes in ice volume, an argument that, until recently, became the general rule in interpreting $\delta^{18}O_b$ records.

Regional changes in deep-water temperature may cause regional differences in $\delta^{18}O_b$ records, obscuring the global signal associated with changes in ice volume. One strategy to account for regional variability and more accurately represent changes in global climate is to stack $\delta^{18}O_b$ records (Imbrie et al., 1984; Prell et al., 1986). The LR04 stack, which is the most comprehensive, shows a glacial–interglacial range of ~ 1.65 per mil over the last few glacial cycles (Fig. 1b) (Lisiecki and Raymo, 2005). Nevertheless, the relative contributions of temperature and ice volume to this stacked record still remain unconstrained, requiring other strategies to isolate the global ice volume signal.

Measurements of the chemistry of pore waters from deep-sea sediments provided the first constraint on the ice-volume contribution to $\delta^{18}O_b$, indicating that $\delta^{18}O_{SW}$ increased by 1.0 ± 0.1 per mil at the Last Glacial Maximum (LGM) (Schrag et al., 1996, 2002). For the total LGM increase of $\delta^{18}O_b$ observed, the residual $\delta^{18}O$ ($\delta^{18}O_b$— $\delta^{18}O_{SW}$) would require that deep-water temperatures decreased nearly to the freezing point (Schrag et al., 1996; Martin et al., 2002). Moreover, a ~ 130 m drop in eustatic sea level at the LGM (Yokoyama et al., 2000) indicates a $\delta^{18}O_{SW}$/sea level relation of ~ 0.008 per mil m^{-1}. Subsequent work indicates that a similar maximum range in $\delta^{18}O_{SW}$ (1.0 ± 0.2 per mil) occurred over the last few glacial cycles (Shackleton, 2000; Lea et al., 2002; Waelbroeck et al., 2002), suggesting that "a substantial portion of the marine 100-kyr cycle…is, in reality, a deep-water temperature signal" (Shackleton, 2000, p. 1899). With a range of 1.65 per mil, for example, the LR04 stack thus indicates a $\sim 60/40$ ice volume/deep-water temperature contribution to the global $\delta^{18}O_b$ signal over the last several glacial cycles, with a globally integrated deep-water cooling of $\sim 2.5\,^{\circ}C$ during glaciations. This is likely the ratio only for glacial maxima, however, as during the course of any given glacial cycle, changes in the $\delta^{18}O$ of the ice sheets (Mix and Ruddiman, 1984; Clarke et al., 2002) would

change the $\delta^{18}O_{SW}$/sea level relation (Waelbroeck et al., 2002).

This issue has a direct bearing on the MPT: how much of the increase in amplitude of the $\delta^{18}O_b$ cycles represents an increase in ice volume relative to additional global cooling of deep-water during glaciations? If we assume a similar contribution of ice volume (60%) and deep-water temperature (40%) to the LR04 stack over the last 2800 ka, then the 41-kyr cycles with < 1 per mil change (Fig. 1b) indicate significantly smaller changes in ice volume than during the 100-kyr cycles with their 1.65 per mil range. Alternatively, if we assume that much of the increase in $\delta^{18}O_b$ across the MPT reflects decreasing glacial deep-water temperatures, then similar changes in ice volume (~ 1 per mil) have occurred throughout the late Pliocene and Pleistocene.

The assumption that similar-volume ($\delta^{18}O_{SW} = 1.0 \pm 0.2$ per mil) ice sheets have occurred over the last 2800 ka requires that, prior to the MPT, no deep-water cooling occurred during the 41-kyr glaciations. Insofar as we know that sea surface temperatures (SSTs) in source regions for North Atlantic Deepwater (NADW) cooled during 41-kyr glaciations (Ruddiman et al., 1989), it seems likely that NADW and much of the deep-ocean throughout the world cooled as well. In support of this, Dwyer et al. (1995) found that North Atlantic bottom water cooled by $\sim 2.3\,^{\circ}C$ during late Pliocene 41-kyr glaciations, suggesting that $\delta^{18}O_{SW}$ at their core site increased by < 0.8 per mil at the same time (Fig. 3c). North Atlantic bottom water cooled an additional $2.2\,^{\circ}C$ during late Pleistocene 100-kyr glaciations, requiring an additional ~ 0.4 per mil increase in $\delta^{18}O_{SW}$ to explain the full amplitude of the $\delta^{18}O_b$ record (Fig. 3a).

The resulting ~ 1.2 per mil range in 100-kyr $\delta^{18}O_{SW}$ ice-volume cycles in the Dwyer et al. data is in good agreement with or slightly higher than independent estimates (Schrag et al., 1996, 2002; Shackleton, 2000). Moreover, application of the $\delta^{18}O_{SW}$/sea level relation (0.008 per mil m^{-1}) to the ~ 0.4 per mil increase in $\delta^{18}O_{SW}$ suggests that post-MPT ice sheets were ~ 50 m larger, in sea-level equivalent, than pre-MPT ice sheets.

Additional support for an increase in ice volume during the MPT comes from shallow marine sediments in Japan, which indicate that eustatic sea level was 20–30 m lower during marine isotope stage 22 relative to stage 28 (Kitamura and Kawagoe, 2006) (Fig. 3b). This lowering coincided with an increase in mean $\delta^{18}O_c$ of ~ 0.18 per mil (Fig. 2b), corresponding to 0.006–0.009 per mil m^{-1} if all attributed to sea level.

The Dwyer et al. (1995) $\delta^{18}O_{SW}$ data also indicate that during glaciations, late Pleistocene North Atlantic bottom water was cooler than during the late Pliocene. Using the constraints imposed by the Dwyer et al. (1995) data on changes in $\delta^{18}O_{SW}$, we use the LR04 stack to evaluate changes in global deep-water temperature. As discussed, a 1 per mil range for 100-kyr $\delta^{18}O_{SW}$ cycles (Schrag et al., 1996, 2002) leaves a residual 0.65 per mil signal in the LR04 stack (Fig. 1b) that reflects global deep-water temperature
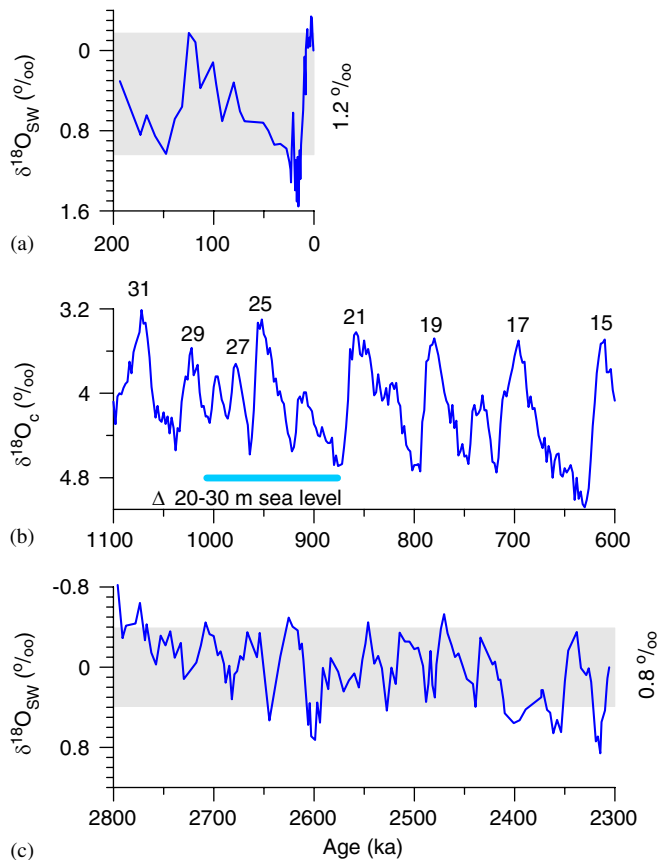
Fig. 3. (a) The $\delta^{18}O_{SW}$ for the last 200 kyr from DSDP Site 607 determined by subtracting the Mg/Ca-temperature component of $\delta^{18}O$ measured on benthic ostracodes (Dwyer et al., 1995), (b) The LR04 $\delta^{18}O_c$ stack for interval 1100-600 ka, showing the interval of a 20–30 m sea-level lowering inferred from sedimentary sequences along the Japan Sea coast (Kitamura and Kawagoe, 2006), (c) The $\delta^{18}O_{SW}$ for the interval 2800–2300 kyr from DSDP Site 607 determined by subtracting the Mg/Ca-temperature component of $\delta^{18}O$ measured on benthic ostracodes (Dwyer et al., 1995).

variability of ~2.6 °C. If, as suggested by the Dwyer et al. data, global ice volume increased by 50% across the MPT, then pre-MPT 41-kyr $\delta^{18}O_{SW}$ cycles had a range of ~0.65 per mil, leaving a residual deep-water signal of ~0.35 per mil (~1.4 °C) in the LR04 stack. This simple analysis thus suggests that the integrated global deep-water temperature may have cooled by an additional ~1.2 °C during 100-kyr glaciations relative to 41-kyr glaciations.

In summary, both ice-volume and deep-water temperature contributions to the LR04 stack likely changed across the MPT, with an increase in ice volume accompanied by a decrease in deep-water temperatures. The details of the trajectory that each component followed, however, remain unclear and await development of a high-resolution record of deep-water temperature during the MPT.

4. Climate change during the MPT

In this section, we examine records (see Fig. 4 for site locations) representing other components of the climate system to characterize any changes in them during the MPT. This examination is far from a complete analysis, and is only intended to provide a first-order description of the nature of any secular and spectral changes in the climate system that may have accompanied the changes in global ice volume that define the MPT. However, given the well-known mechanisms by which ice sheets directly influence climate (Clark et al., 1999), including possibly being an amplifier or driver of the 100-kyr cycle, we expect some changes of other components of the climate system to occur in response to changes in global ice volume.

Before proceeding, however, it is important to emphasize two important caveats with respect to interpreting orbital-scale climate change from long time series. The first has to do with age models, with the convention being to tune a $\delta^{18}O$ record to orbital parameters (Imbrie et al., 1984; Shackleton et al., 1990), thus introducing a potential systematic bias in the distribution of spectral power for a given climate record. Huybers and Wunsch (2004) have developed new strategies for constructing age models independent of such tuning procedures, but nearly all of the records evaluated herein are based on orbitally tuned age models, and the potential bias in spectral power must be kept in mind. The second caveat has to do with interpreting phase relations between $\delta^{18}O_b$ and other proxies measured in the same core. The issue here has to do with assuming that $\delta^{18}O_b$ is a strict measure of ice volume, whereas it is increasingly clear that deep-water temperatures and other watermass effects may contribute a significant fraction of this signal (e.g., Shackleton, 2000), that changes in ice isotopic composition may systematically shift the phase of $\delta^{18}O_b$ (Mix and Ruddiman, 1984), and that as a result the ice volume and isotope signals do not covary at all times (Clark and Mix, 2000; Skinner and Shackleton, 2005). Accordingly, phasing arguments based solely on $\delta^{18}O_b$ must be considered tentative until a record of $\delta^{18}O_{SW}$ is developed that firmly establishes the phasing of variations in ice volume with respect to other components of the climate system.

4.1. SSTs

We first examine records of SSTs from the Atlantic basin. The Atlantic meridional overturning circulation (AMOC) associated with North Atlantic Deepwater formation (NADW) induces northerly, cross-equatorial heat transport in the Atlantic basin. Accordingly, a component of changes in southern and tropical Atlantic SSTs may be inversely related to changes in North Atlantic SSTs through a change in the AMOC (Mix et al., 1986; Crowley, 1992). SST changes in the tropical Atlantic may also be induced by changes in upwelling, while SSTs in the South Atlantic may occur in response to changes in the position of the westerlies or the extent of sea ice.

An estimation of North Atlantic SSTs (DSDP Site 607, 41 °N) based on census counts (Ruddiman et al., 1989) indicates that a general cooling of the North Atlantic began
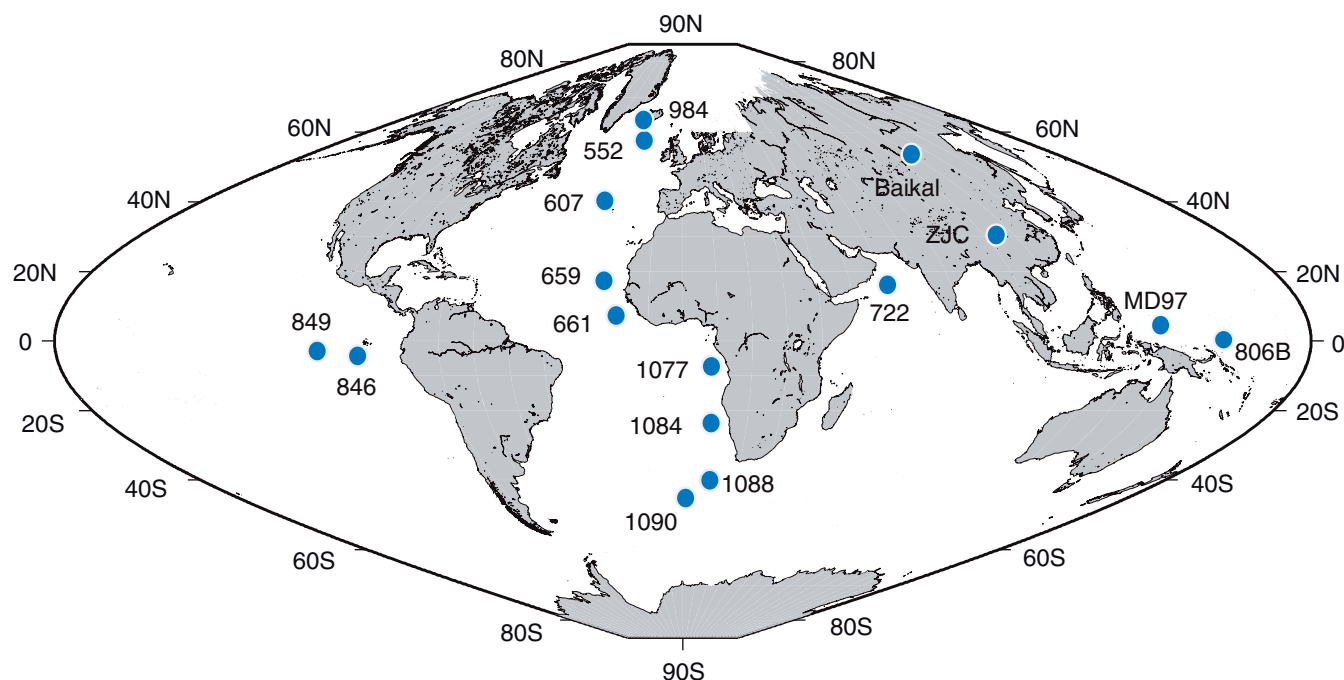
Fig. 4. Location of sites with long time series of climate variables discussed in text.

at the onset of the MPT, with SSTs reaching minimum values by ∼900 ka, corresponding to a net cooling of ∼9 °C (Fig. 5a). SSTs then began to increase through the remainder of the MPT, reaching an average value ∼2 °C cooler than before the MPT. To a large extent, however, the form of this MPT SST oscillation is determined by a substantial cooling event at ∼900 ka. On one hand, this event may be the culmination of the cooling trend that began at the start of the MPT. Alternatively, it may be a unique event that, if excluded from the record, would suggest a secular 3–4 °C MPT cooling that stabilized at a new, lower SST by 900 ka. In view of further evidence discussed below, we believe that the latter scenario is the more likely, and we return to this "900-ka event" in greater detail below.

Schefus et al. (2004) developed an alkenone record of eastern tropical Atlantic SSTs off the west coast of Africa (ODP Site 1077, 10°26′S) that spans the MPT (Fig. 5b). This record is characterized by relatively brief intervals of glacial cooling and long interglaciations, with a prominent cooling event centered on 900 ka that is distinguished from other glacial events in this record by its duration and extent of cooling. In this record, average tropical Atlantic SSTs returned to their previously warm state following the MPT.

Marlow et al. (2000) developed a low-resolution (∼50 kyr sample interval) alkenone record of SSTs from the Benguela Current upwelling system off the southwest coast of Africa (Site 1084, 25°31′S) (Fig. 5c). For ∼800 kyr prior to the MPT, SSTs in the Benguela Current were stable, averaging ∼20 °C. A secular cooling of 5 °C then began at the start of the MPT and was complete by ∼850 ka, with no further long-term change in SSTs.

Becquey and Gersonde (2002) developed a record of South Atlantic summer SSTs (Site 1090, 42°55′S) using the Modern Analog Technique applied to planktonic foraminifera (Fig. 5d). Because the core site lies between the modern positions of the Subantarctic and Subtropical fronts, changes in SSTs at this site monitor meridional changes in the position of oceanographic fronts in the Southern Ocean. Early Pleistocene (1800–870 ka) SSTs averaged ∼4 °C with small glacial–interglacial variability, indicating a northward shift of the Polar Front by at least 7° from its present position. Beginning at 870 ka, glacial–interglacial variability began to increase, primarily in response to increasing interglacial SSTs that approached or exceeded modern values (10 °C) (Fig. 5d).

Several newly developed SST records document a significant change in the tropical Pacific Ocean during the MPT. The tropical Pacific Ocean is characterized by zonal SST and pressure gradients associated with a westerly dipping thermocline, with shallower thermocline depths in the eastern Pacific induced by wind-driven upwelling and shallow meridional transport of subducted extratropical waters. The zonal SST and pressure gradients affect the strength of the easterly trade winds, providing a positive feedback to the maintenance of the gradients. Accordingly, any forcing that may cause a change in the slope of the thermocline will lead to a change in the zonal gradients and an attendant change in the winds, further changing the gradients.

SST records from the equatorial Pacific indicate that zonal SST gradients (and thus pressure gradients) increased during the MPT (Fig. 6). Two alkenone-derived SST records from the eastern equatorial Pacific (Site 846, 3°5′S; Liu and Herbert, 2004) (Site 849, 0°11′N;
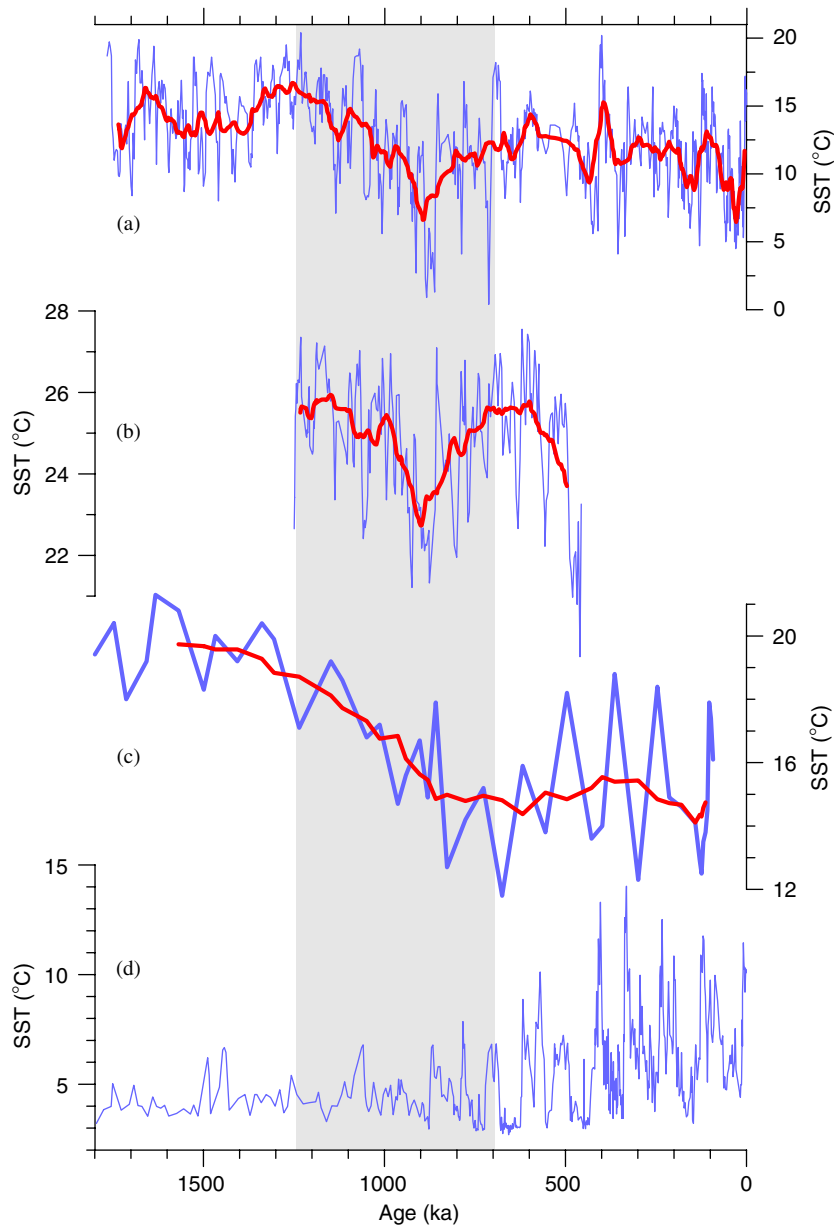
Fig. 5. (a) North Atlantic SSTs (blue line) from DSDP Site 607 (41°N) based on census counts of foraminifera (Ruddiman et al., 1989). Thick red line is running average of the data, (b) Alkenone record of eastern tropical Atlantic SSTs (blue line) off the west coast of Africa (ODP Site 1077, 10°26'S) (Schefus et al., 2004). Thick red line is running average of the data, (c) Alkenone record of SSTs (blue line) from the Benguela Current upwelling system off the southwest coast of Africa (ODP Site 1084, 25°31'S) (Marlow et al., 2000). Thick red line is running average of the data, (d) Summer South Atlantic SSTs (ODP Site 1090, 42°55'S) based on the Modern Analog Technique applied to planktonic foraminfera (Becquey and Gersonde, 2002). Broad light-gray vertical bar shows timing of the MPT (Fig. 2). All records are shown on their published age models.

McClymont and Rossel-Mele, 2005) indicate a 1.5 °C secular cooling from the start of the MPT until 900 ka, with subsequent average SSTs then remaining unchanged (Fig. 6a, b). In contrast, two SST records from the western equatorial Pacific (core MD97-2140, 2°02'N; de Garidel-Thoron et al., 2005) (Site 806B, 0°19'N; Medina-Elizalde and Lea, 2005) suggest that long-term average SSTs of the Western Pacific Warm Pool changed relatively little through the Pleistocene, with no systematic shift across the MPT (Fig. 6c, d).

We use time–frequency spectrograms (moving window Fourier transform) of the most complete time series to examine the spectral evolution of SSTs during the Pleistocene (Fig. 7). The North Atlantic SST record clearly shows the emergence of low-frequency power (~100 kyr) at the start of the MPT (Fig. 7a), reflecting the sensitivity of this region to ice-sheet influences (Ruddiman and McIntyre, 1981; Ruddiman et al., 1989). As is the case with all spectrograms examined herein, however, including the LR04 δ^{18}O record (Fig. 2), this low-frequency
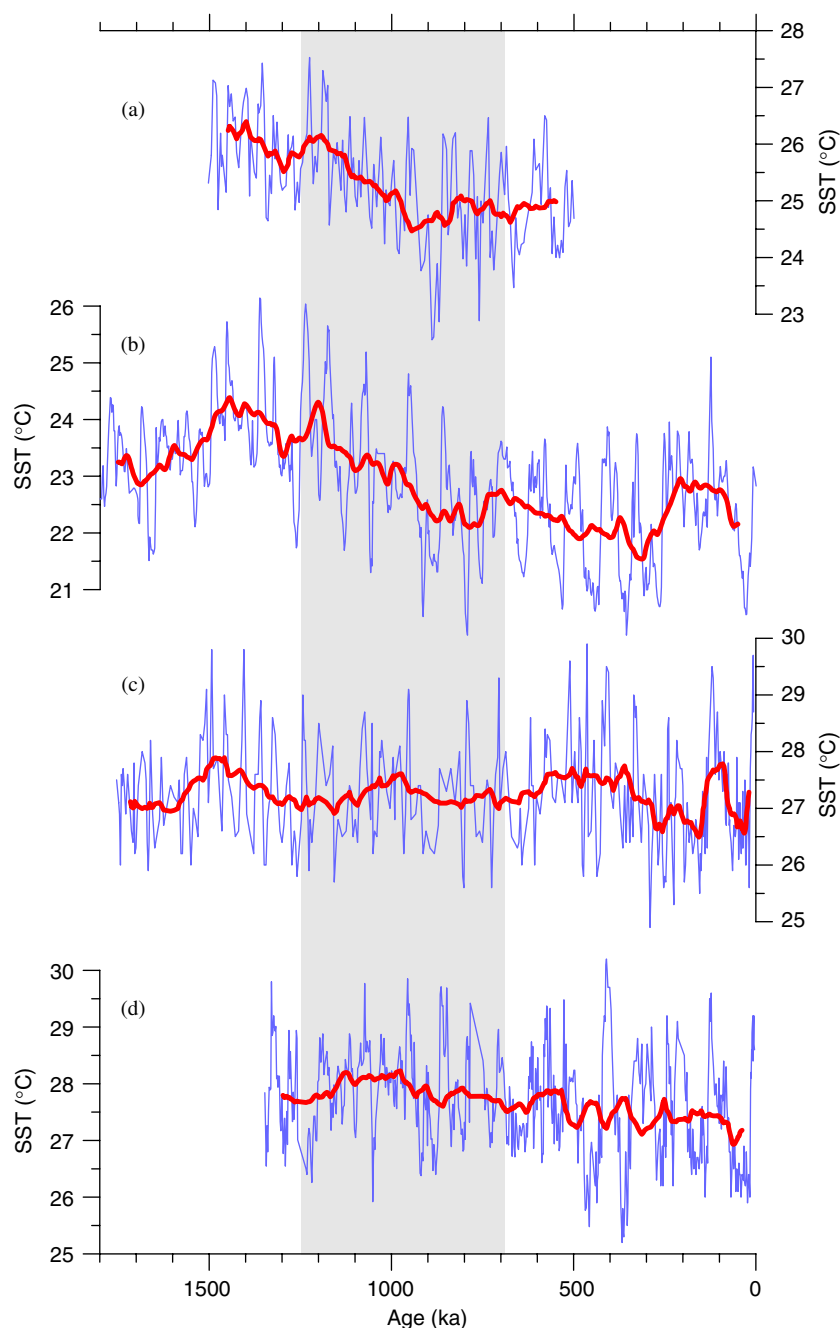
Fig. 6. (a) Alkenone record of SSTs (blue line) from the eastern equatorial Pacific (ODP Site 849, 0°11'N) (McClymont and Rossel-Mele, 2005). Thick red line is running average of the data, (b) Alkenone record of SSTs (blue line) from the eastern equatorial Pacific (ODP Site 846, 3°5'S) (Liu and Herbert, 2004). Thick red line is running average of the data, (c) Alkenone record of SSTs (blue line) from the western equatorial Pacific (core MD97-2140, 2°02'N) (de Garidel-Thoron et al., 2005). Thick red line is running average of the data, (d) Mg/Ca record of SSTs from the western equatorial Pacific (ODP Site 806B, 0°19'N) (Medina-Elizalde and Lea, 2005). Thick red line is running average of the data. Broad light-gray vertical bar shows timing of the MPT (Fig. 2). All records are shown on their published age models.

component exhibits substantial variability through time, both in frequency and amplitude. With respect to frequency, this component is best described as a broad band between 0.015 and 0.005 kyr^{-1} (66–200 kyr), rather than as a narrow and persistent 100-kyr band. With respect to amplitude, the low-frequency component increases and decreases in relative power, and shared intervals of high or low power among the time series are uncommon.

A component of low-frequency variance (> 100 kyr) is present throughout the SST record from the eastern equatorial Pacific (and this is also found in varying biogenic sedimentation rates, Mix et al., 1995a), although this variability shifts phase and becomes centered on ~100 kyr and begins to mimic δ^{18}O starting at ~950 ka (Fig. 7b) (Liu and Herbert, 2004). In comparison, spectrograms of the two western equatorial Pacific SST records
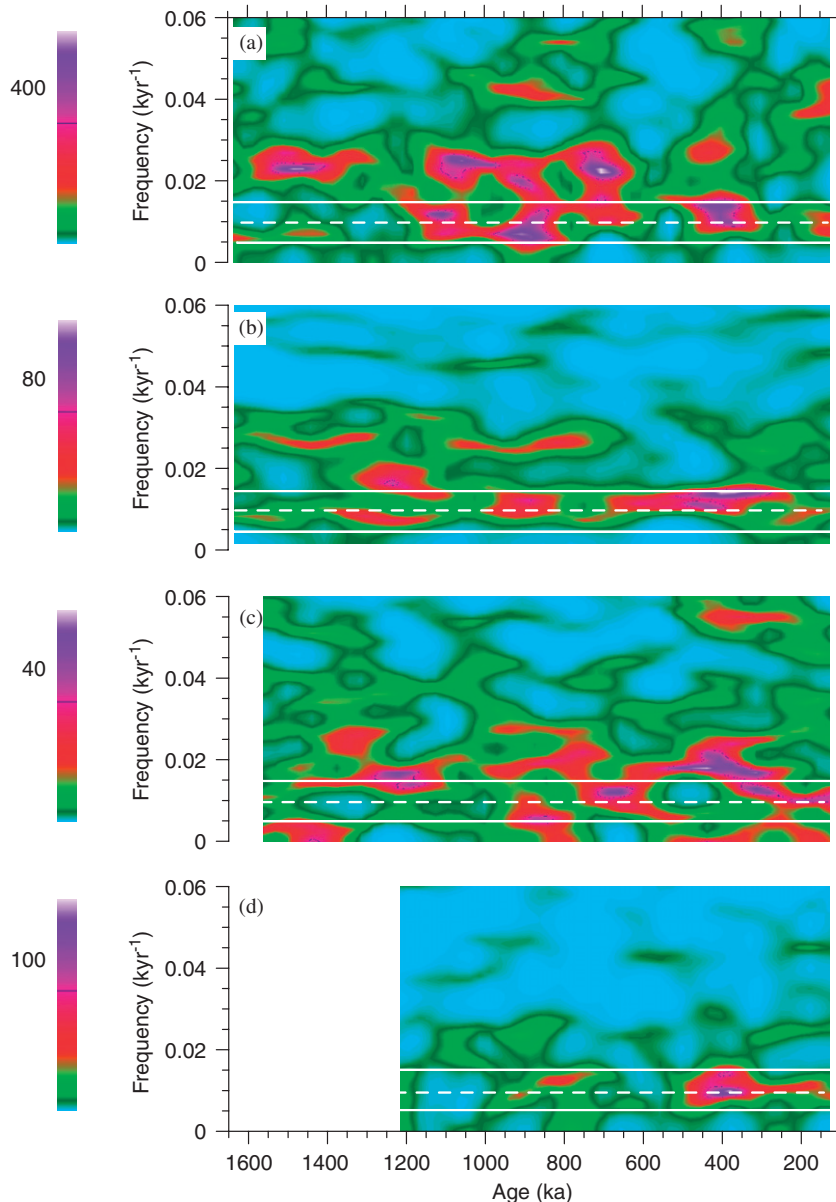
Fig. 7. Time-frequency spectrograms (moving window Fourier transform) showing the distribution of signal power (cycles/kyr) in SST records. Relative power shown by color bars; note different color scales. All time series were detrended, tapered, and filtered forwards and backwards to minimize any phase shift due to the filter. (a) Spectrogram of SST record from DSDP Site 607 (41°N) (Ruddiman et al., 1989) (window length = 250 kyr, sliding window length = 25 kyr, high-pass filter with corner frequency 0.0025), (b) Spectrogram of SST record from ODP Site 846 (3°5′S) (Liu and Herbert, 2004) (window length = 325 kyr, sliding window length = 33 kyr, high-pass filter with corner frequency 0.0025), (c) Spectrogram of SST record from core MD97-2140 (2°02′N) (de Garidel-Thoron et al., 2005) (window length = 300 kyr, sliding window length = 30 kyr, data interpolated at 1.0 kyr intervals, high-pass filter with corner frequency 0.0025), (d) Spectrogram of SST record from ODP Site 806B (0°19′N) (Medina-Elizalde and Lea, 2005) (window length = 250 kyr, sliding window length = 25 kyr, data interpolated at 0.5 kyr, high-pass filter with corner frequency 0.0025). All records are shown on their published age models.

(Fig. 7c, d) exhibit no low-frequency variance prior to 950 ka, but its subsequent emergence indicates a basin-wide response at this time. All Pacific records exhibit relatively high spectral power within the time interval of the MPT at ~900 ka, which is also seen in the North Atlantic SST record (Fig. 7a). This maximum corresponds to the cold SST event at 900 ka (Fig. 5), and reflects the longer duration of this event relative to other glacial events during the MPT. The only other interval of general agreement

among the records occurs 400 ka (isotope stage 11), when a peak in low-frequency spectral is present in all but the MD97-2140 record.

4.2. Asian and African monsoons and aridity

We next summarize proxies representing changes in monsoon strength and aridity of Asia and Africa. Monsoons develop in response to the seasonal contrasts

in land-sea heating. In boreal winter, high-pressure systems develop over the cooler Asian and African landmasses, and attendant offshore winds deliver continental dust to the adjacent Atlantic and Indian oceans. In boreal summer, differential heating of the continents induces development of low pressure, resulting in a reversal of the wind fields and attendant onshore moisture transport. Latent heat released during precipitation over land acts as a positive feedback that helps to fuel the summer monsoon circulation. Longer-timescale variations in monsoon dynamics occur when any forcing causes a change in the differential heating of the continents and oceans, leading to a change in the intensity of the summer monsoon relative to the winter monsoon. To a first order, these long-term changes in monsoonal strength cause changes in aridity, with intervals of enhanced winter (summer) monsoons associated with drier (wetter) conditions.

The percent and flux of eolian sediments to adjacent oceans is a proxy for aridity of the source area (Tiedemann et al., 1994; deMenocal, 1995; Clemens et al., 1996), whereas monsoon wind strength can be estimated from the grain size of wind-blown lithogenic sediments deposited in the oceans and on the loess plateau of China (Clemens et al., 1996; Sun et al., 2006). Lastly, Williams et al. (1997) interpret the sedimentary record of biogenic silica in Lake Baikal, south-central Siberia, as a proxy for temperature, with high biogenic silica percentages associated with warmer waters in the lake. Insofar as temperatures over Asia affect the strength of the Asian monsoon, then the Baikal record can also be interpreted as one of changing monsoonal strength.

The percent of eolian sediments in marine cores off the eastern equatorial Atlantic (ODP Sites 659, 661) show no secular changes during the MPT (Fig. 8a) (deMenocal, 1995). In contrast, the flux of eolian sediments suggests an increase in the aridity of West African source regions (Sahara and Sahel) ~1500 ka (Fig. 8b). Similarly, ODP Site 722 in the Arabian Sea indicates no change in the percent of dust derived from northeast African and Arabian sources associated with Indian monsoon surface winds (not shown), but an increase in eolian flux is clearly apparent at ~1350 ka (Fig. 8c) (Clemens et al., 1996). Sun et al. (2006) interpret the Chinese loess grain size record to identify an increase in the mean intensity and amplitude of the winter monsoon at the start of the MPT (Fig. 8d). Lastly, the Lake Baikal record suggests that biogenic silica (and thus central Asian temperature) increased during interglaciations at the start of the MPT (Williams et al., 1997) (Fig. 8e).

Spectrograms of percent African-derived eolian dust from ODP Sites 659 and 661 (not shown) document the presence of low-frequency variability throughout the last 3 Myr. In contrast, spectrograms of eolian flux from ODP Site 659 (Fig. 9a) and ODP Site 722 (Fig. 9b), grain size from Chinese loess (Fig. 9c), and Lake Baikal biogenic silica (Fig. 9d) indicate the emergence of low-frequency variability in African aridity ~100 kyr before the start of

the MPT, with a maximum in variance in all records but ODP 722 coincident with the start of the MPT. The only other interval with a shared maximum in low-frequency variance occurs at 400-450 ka (isotope stages 11 and 12).

4.3. Deep-ocean circulation

Shackleton (1977) pioneered the use of geochemical tracers of deep-ocean nutrient distributions, primarily $\delta^{13}C$ of dissolved inorganic carbon (DIC), to monitor transfers of carbon between the organic pool (especially in continental biomass) and the inorganic pool (primarily carbonate and bicarbonate ions) in the ocean, and Shackleton et al. (1983) first employed carbon isotope gradients to examine past variations in deep-water circulation. Surface-water productivity strips from the water isotopically light carbon and nutrients, and carbon isotopic fractionation during air–sea exchange causes DIC to be enriched in ^{13}C relative to atmospheric CO_2, with a temperature dependency of ~0.1 per mil enrichment per degree of cooling (Broecker and Maier-Reimer, 1992). Accordingly, the preformed properties of newly formed deep-water, including its $\delta^{13}C$ value, will reflect a balance of effects related to rapid biological utilization and export of nutrients and carbon, and slower air–sea gas exchange. Because the carbon and nutrients accumulate in deep-water over time through respiration of sinking organic matter, newly formed deep-waters can be distinguished from older deep-water from the same source by their relatively high $\delta^{13}C$ values and low nutrient contents.

The two primary surface-water sources of global deep-water formation today have preformed $\delta^{13}C$ values that can be readily distinguished from each other. North Atlantic Deepwater (NADW) formed from near-surface waters that have largely equilibrated with the atmosphere, and have relatively low preformed nutrients, both of which yield high preformed $\delta^{13}C$ values of 1.0–1.5 per mil. Deep-water formed around the Antarctic continent originates from deeper upwelled waters that were exposed only briefly at the surface (and in a region of limited gas exchange due to sea-ice cover) and have relatively high preformed nutrients, resulting in preformed $\delta^{13}C$ values of ~0.3 per mil. These two water masses mix around the Antarctic continent and fill the deep Pacific basin, where, through further aging, the $\delta^{13}C$ of DIC further decreases.

Changes in the volume of deep-water masses with differing origins can be reconstructed from time series of $\delta^{13}C$. In the Atlantic basin, denser Circumpolar Deep-water (CDW) with its distinctive low $\delta^{13}C$ values underlies less dense NADW with its distinctive higher $\delta^{13}C$ values. Changes in the position of the mixing front between the two water masses reflect some combination of changes in their density and rate of formation. Independent tracers generally support the first-order approximation that temporal changes in deep Atlantic $\delta^{13}C$ correspond qualitatively to changes in the rate of NADW formation during the last glacial cycle (McManus et al., 2004).
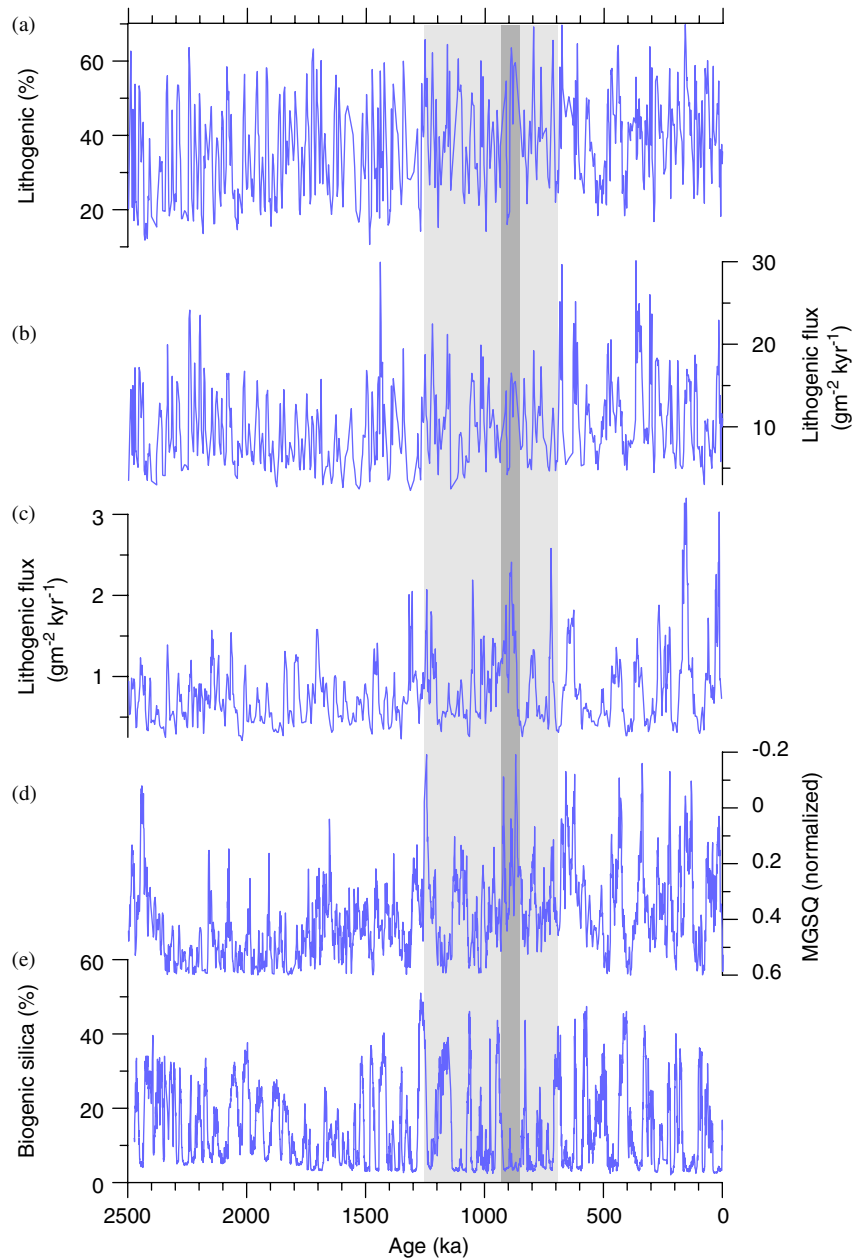
Fig. 8. (a) Percent terrigenous (eolian) sediments in ODP Site 659 (deMenocal, 1995), (b) Flux of terrigenous (eolian) sediments in ODP Site 659 (Tiedemann et al., 1994), (c) Flux of terrigenous (eolian) sediments in ODP Site 722 (Clemens et al., 1996), (d) Stacked record of normalized mean grain size of quartz (MGSQ) from loess sequences on the Chinese Loess Plateau (Sun et al., 2006), (e) Percent biogenic silica from Lake Baikal, south-central Siberia (Williams et al., 1997). Broad light-gray vertical bar shows timing of the MPT (Fig. 2). Narrow darker gray vertical bar shows timing of 900-ka event (see text for discussion). All records are shown on their published age models.

We first discuss $\delta^{13}C$ records from the Atlantic and Pacific basins that suggest significant changes in deep-ocean circulation during the MPT. In order to account for global ocean $\delta^{13}C$ variations associated with changes in the carbon cycle, we follow the approach of Shackleton et al. (1983) by calculating interocean and vertical $\delta^{13}C$ gradients to estimate the relative strengths of deep-water formation (Raymo et al., 1990, 2004; Mix et al., 1995b).

The $\delta^{13}C$ record from DSDP Site 607 (Fig. 10a) lies at the core of modern NADW, and thus monitors changes in the relative strength of NADW versus CDW (Raymo et al.,

1990). What is immediately apparent from this record is the change in the mean and variability prior to $(0.81 \pm 0.30\,\text{‰})$ relative to after $(0.43 \pm 0.50\,\text{‰})$ the MPT, changes that are primarily associated with more depleted glacial $\delta^{13}C$ values (Fig. 10a). Following Mix et al. (1995b), we account for global ocean $\delta^{13}C$ variations associated with changes in the carbon cycle by calculating the Atlantic–Pacific $\delta^{13}C$ gradient $(\Delta\delta^{13}C_{(A-P)})$ through the last 2 Myr using $\delta^{13}C$ values from Pacific Site 849 (0°11′N, 3851 m water depth) (Fig. 10c). In this $\Delta\delta^{13}C_{(A-P)}$ record, the change to more depleted glacial $\delta^{13}C$ values seen in the Site 607 record at
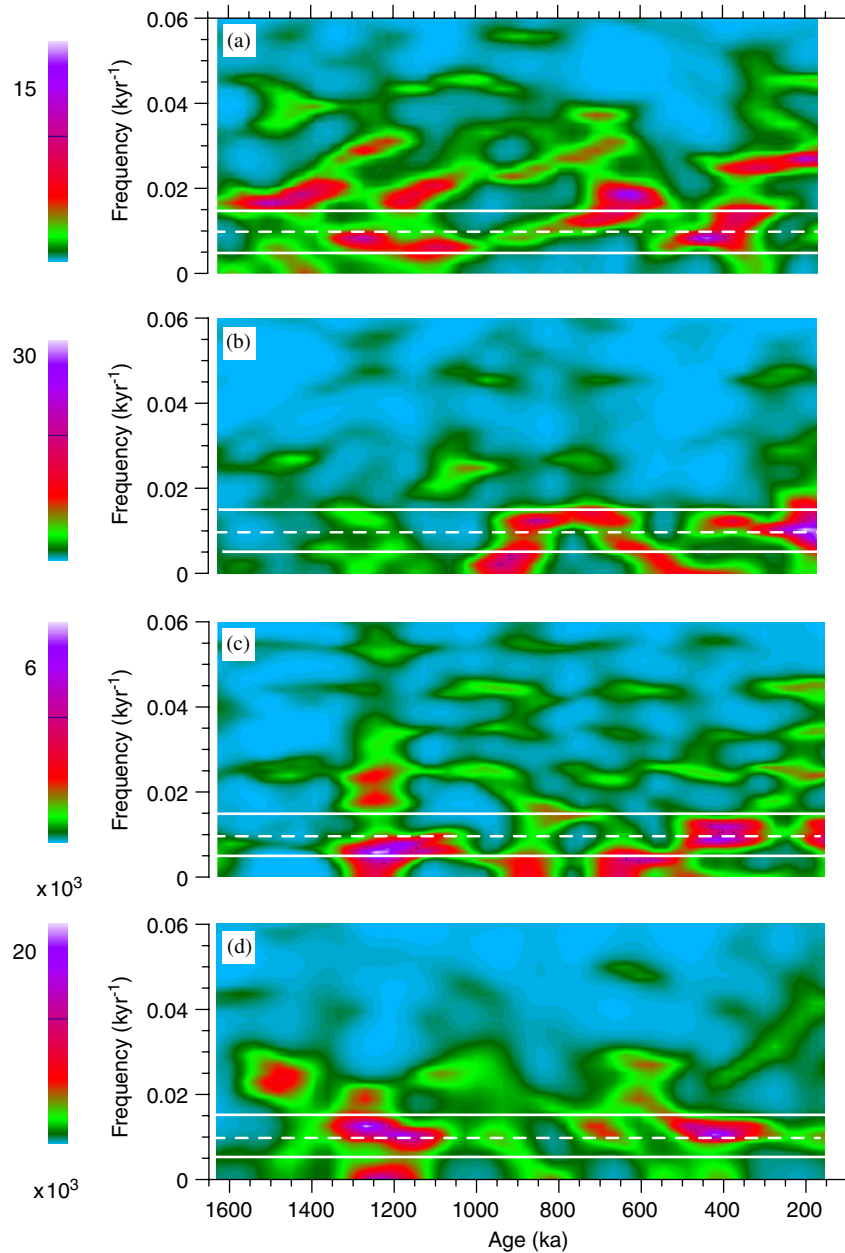
Fig. 9. Time-frequency spectrograms (moving window Fourier transform) showing the distribution of signal power (cycles/kyr) in records of African and Asian aridity and monsoon intensity. Relative power shown by color bars. All time series were detrended, tapered, and filtered forwards and backwards to minimize any phase shift due to the filter. (a) Spectrogram of lithogenic flux from ODP Site 659 (Tiedemann et al., 1994) (window length = 300 kyr, sliding window length = 30 kyr, data interpolated at 0.5 kyr, high-pass filter with corner frequency 0.00125), (b) Spectrogram of lithogenic flux from ODP Site 722 (Clemens et al., 1996) (window length = 300 kyr, sliding window length = 30 kyr, data interpolated at 0.5 kyr, high-pass filter with corner frequency 0.00125), (c) Spectrogram of stacked mean grain size record from Chinese Loess Plateau (Sun et al., 2006) (window length = 300 kyr, sliding window length = 30 kyr, data interpolated at 1.0 kyr, high-pass filter with corner frequency 0.0025), (d) Spectrogram of percent biogenic silica from Lake Baikal, south-central Siberia (Williams et al., 1997) (window length = 300 kyr, sliding window length = 30 kyr, data interpolated at 0.5 kyr, high-pass filter with corner frequency 0.0025). All records are shown on their published age models.

the start of the MPT is reflected by decrease in the $\Delta\delta^{13}C_{(A-P)}$ gradient, which falls abruptly starting at ~1250 ka and vanished during glaciations starting at ~900 ka (Fig. 10d).

ODP Site 1090 lies near the distal interface of modern NADW with CDW, but given its southerly location (43°S) and great water depth (3702 m), changes in $\delta^{13}C$ at this site primarily reflect changes in preformed properties of CDW (Hodell et al., 2003). This record shares with North Atlantic Site 607 a decrease in glacial $\delta^{13}C$ values at the onset of the MPT, causing a similar decrease in the mean and increase in the range of glacial–interglacial variations (-0.12 ± 0.44‰ before, -0.54 ± 0.56‰ after) (Fig. 10b).
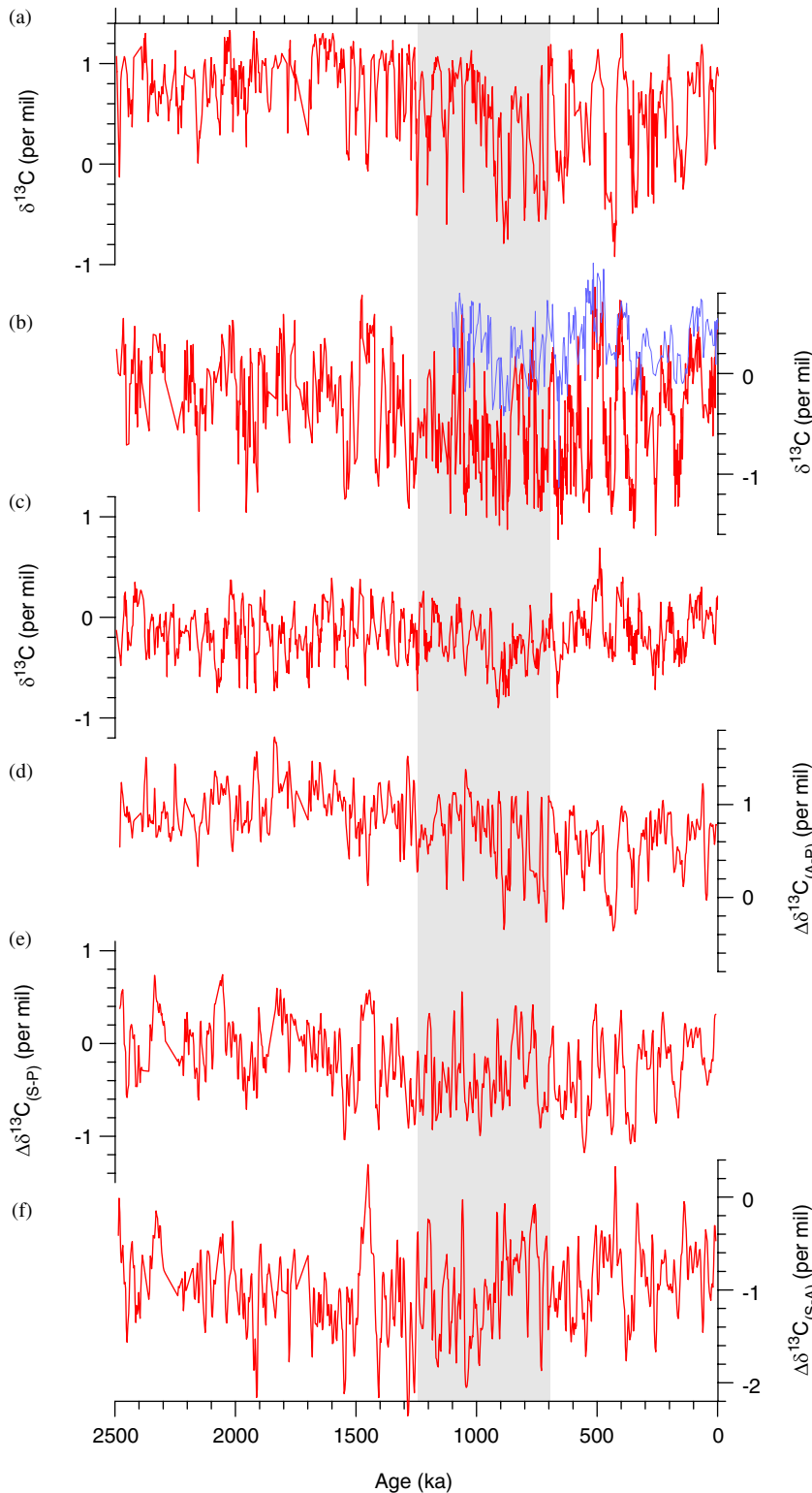
Fig. 10. (a) $\delta^{13}C$ record measured on *Cibicidoides wuellerstorfi* from DSDP Site 607 (Raymo et al., 1990, with age model transferred to the LR04 stack by M. Raymo, personal communication), (b) $\delta^{13}C$ record measured on *Cibicidoides wuellerstorfi* from ODP Site 1090 (in red) and ODP Site 1088 (in blue) (Hodell et al., 2003), (c) $\delta^{13}C$ record measured on *Cibicidoides wuellerstorfi* from ODP Site 849 (Mix et al., 1995a,b), (d) The $\delta^{13}C$ gradient ($\Delta\delta^{13}C_{(A-P)}$) between North Atlantic DSDP Site 607 (Raymo et al., 1990) and Pacific ODP Site 849 (Mix et al., 1995a,b), (e) The $\delta^{13}C$ gradient ($\Delta\delta^{13}C_{(S-P)}$) between South Atlantic ODP Site 1090 (Hodell et al., 2003) and Pacific ODP Site 849 (Mix et al., 1995a,b), (f) The $\delta^{13}C$ gradient ($\Delta\delta^{13}C_{(S-A)}$) between South Atlantic ODP Site 1090 (Hodell et al., 2003) and North Atlantic DSDP Site 607 (Raymo et al., 1990). Broad light-gray vertical bar shows timing of the MPT (Fig. 2). All records are shown on their published age models.

Based on a lower resolution and less complete record from the subAntarctic, Mix et al. (1995b) noted that the $\Delta\delta^{13}C_{(S-P)}$ record contrasts with the $\Delta\delta^{13}C_{(A-P)}$ record in having much lower or even negative $\delta^{13}C$ gradients, a finding consistent with the $\Delta\delta^{13}C_{(S-P)}$ record presented here (Fig. 10e) based on a longer and higher resolution subAntarctic $\delta^{13}C$ record from ODP Site 1090 (Hodell et al., 2003). Mix et al. (1995b) concluded that these differences suggest little or no export of NADW to CDW, and the $\Delta\delta^{13}C_{(S-P)}$ signal is instead driven by changes originating in the Southern Ocean. Hodell et al. (2003) provided further insight into this issue by using a mid-depth $\delta^{13}C$ record from Site 1088 (41°S, 2100 m water depth) (Fig. 10b, blue curve) with the Site 1090 $\delta^{13}C$ record (Fig. 10b, red curve) to show that vertical $\delta^{13}C$ gradients steepened considerably during glaciations of the last 1000 kyr, indicating a persistent source of intermediate water enriched in $\delta^{13}C$, but changes in $\delta^{13}C$ of CDW driven by variability in the ventilation of CDW rather than mixing with NADW. Toggweiler (1999) proposed one possible mechanism to explain changes in CDW ventilation, whereby a change in circulation that isolates CDW from intermediate water would occur in association with a shift in mid-latitude westerlies toward the equator and attendant weakening of wind-driven upwelling.

Mix et al. (1995b) also argued that the more negative Antarctic $\delta^{13}C$ glacial values relative to Pacific glacial values requires either a different source of low-nutrient and/or high preformed $\delta^{13}C$ Pacific deep-water or isolation of circumpolar waters from Pacific waters so that they acted as a nutrient trap. We note that the change to a more negative gradient at the start of the MPT would require that these possible controls became more effective at that time. An additional control associated with the start of the MPT that would have affected the ocean $\delta^{13}C$ budget may have been the transfer of depleted terrestrial carbon to the ocean in response to increasing aridity (Fig. 8).

Raymo et al. (1990) argued that the MPT change to more depleted glacial $\delta^{13}C$ at Site 607 (and a decrease in the $\Delta\delta^{13}C_{(A-P)}$ signal) represented a weakening of NADW formation during glaciations, allowing greater penetration of depleted CPW into the North Atlantic basin. More recently, Raymo et al. (2004) argued that the progressive depletion of $\delta^{13}C$ in the Site 607 record may reflect instead a greater influence of CDW. Support for this latter argument comes from the intra-Atlantic $\delta^{13}C$ gradient ($\Delta\delta^{13}C_{(S-A)}$) derived by subtracting the Site 607 $\delta^{13}C$ values from Site 1090 $\delta^{13}C$ values (Fig. 10f). In particular, the average $\Delta\delta^{13}C_{(S-A)}$ signal remains constant throughout the Pleistocene, suggesting that the depletion in glacial $\delta^{13}C$ seen in both records at the start of the MPT is related to a change in the ventilation of CDW.

Raymo et al. (2004) further examined changes in the history of NADW formation by reconstructing vertical (depth) gradients of $\delta^{13}C$ in the North Atlantic using 10,000-yr averaged $\delta^{13}C$ values representing glaciations and interglaciations over the last 1800 ka. The classic picture that has evolved since the work of Boyle and Keigwin (1987) and Duplessy et al. (1988) is one of the present interglaciation as having little to no $\delta^{13}C$ gradient, reflecting the penetration of NADW to the abyss, versus the LGM 21 ka having a positive $\delta^{13}C$ gradient, suggesting that the North Atlantic was stratified with a divide at ~2000 m separating enriched Glacial North Atlantic Intermediate Water from underlying depleted CDW. The Raymo et al. (2004) analysis, however, found that glacial–interglacial $\delta^{13}C$ gradients over the last 1800 kyr often differed from this picture, with the most recent examples being relatively unique. Instead, the "typical" vertical $\delta^{13}C$ gradient, characteristic of both glaciations and interglaciations, is negative, implying a source of depleted $\delta^{13}C$ water in the North Atlantic. Raymo et al. (2004) speculate that such a source was from brine formation beneath permanent sea ice covering the Norwegian-Greenland Seas, with depleted $\delta^{13}C$ values reflecting an attendant reduction in air–sea exchange.

We have further evaluated this hypothesis by subtracting $\delta^{13}C$ values measured on Site 607 (3427 m water depth) from the intermediate-depth site that recorded the most depleted $\delta^{13}C$ values in the Raymo et al. (2004) analysis (ODP Site 984, 61°N, 1650 m water depth) in order to construct a continuous time series of changes in the vertical (depth) North Atlantic $\delta^{13}C$ gradient ($\Delta\delta^{13}C_{(I-D)}$). This record indicates that a significant change in the average vertical $\delta^{13}C$ structure of the North Atlantic occurred at ~900 ka when glacial gradients shifted from near-zero to more positive values like that of the last glaciation (Fig. 11a, red line). Interglacial gradients, on the other hand, remained reversed until ~500 ka when, with the exception of the stage 11, they switched to a near-zero value like that of the present interglaciation. Because the glacial $\delta^{13}C$ values of intermediate waters sampled by Site 984 do not change in the early part of the record (Raymo et al., 2004), the increase in glacial gradients at 900 ka reflects the change to more depleted $\delta^{13}C$ values of deep-water at Site 607, which we attribute to a change in CDW. Interglacial gradients, on the other hand, decrease at 500 ka because of a marked enrichment of $\delta^{13}C$ values in the Site 984 record at that time (Raymo et al., 2004).

The $\Delta\delta^{13}C_{(I-D)}$ signal also indicates that prior to 900 ka, variability in the $\Delta\delta^{13}C_{(I-D)}$ signal was uncorrelated with ice volume (Fig. 11b), whereas it became highly correlated after that time (Fig. 11c). We suggest that prior to 900 ka, the two records may be out of phase, with changes in the gradient reflecting North Atlantic intermediate water variability that is independent of CDW variability. Subsequent correlation then suggests that the onset of a strong and persistent ~100-kyr ice-volume cycle at 900 ka (Fig. 2f) synchronizes the variability of the two water masses.

Additional support for this argument is derived from spectrograms of the three main $\delta^{13}C$ sites (607, 1090, 849) monitoring deep-ocean circulation, which show the emergence of low-frequency power ~900 ka (Fig. 12). Sites 849 and 1090 also exhibit some intervals of low-frequency
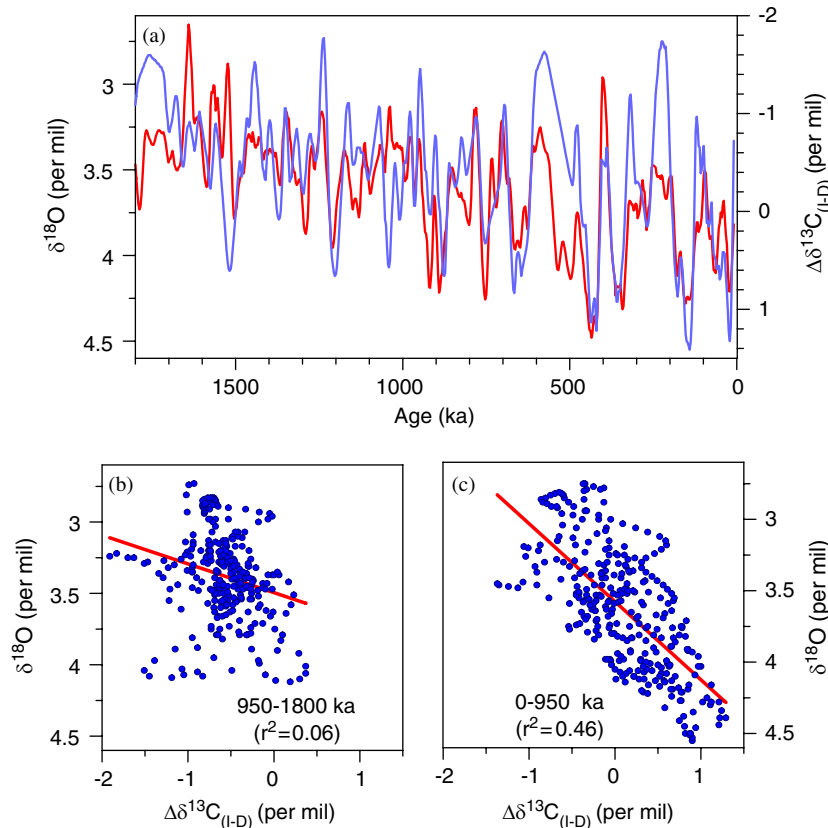
Fig. 11. (a) The $\delta^{18}O_b$ record (in blue) from ODP Site 984 (Raymo et al., 2004), and the vertical $\delta^{13}C$ gradient ($\Delta\delta^{13}C_{(I-D)}$) (in red) derived by subtracting the Site 607 $\delta^{13}C$ record from the Site 984 $\delta^{13}C$ record, (b) The relation between the Site 984 $\delta^{18}O_b$ record and the $\Delta\delta^{13}C_{(I-D)}$ for the interval 950-1800 ka, (c) The relation between the Site 984 $\delta^{18}O_b$ record and the $\Delta\delta^{13}C_{(I-D)}$ for the interval 0-950 ka. All records are shown on their published age models.

power earlier in the Pleistocene, but 900 ka stands out as a time when a low-frequency component appears as a consistent feature in all three records. Similar to other climate records discussed above, however, the low-frequency component does not have a persistent concentration of variance at 100 kyr (Mix et al., 1995b), and regardless of the frequency, the relative power varies through time. We note that all three records show a maximum in 100-kyr variance between 400 and 500 ka, suggesting an especially well-organized global response at that time.

4.4. The 900-ka event

As inferred throughout the above discussion, 900 ka (corresponding to marine isotope stages 22 and 24) stands out in many climate records as an event as well as a turning point both in the time and frequency domain. As defined by changes in ice volume, the MPT began 1250 ka with a gradual increase in the long-term average, accompanied by an increase in the amplitude of variability, with these changes reaching completion by 700 ka. However, the first long (~80 kyr) glaciation of the Pleistocene occurs in the LR04 $\delta^{18}O$ stack at 900 ka, with marine isotope stages 24 and 22 separated by a subdued stage 23 giving rise to a structure similar in many ways to that of the last glacial

cycle (stages 2, 3 and 4) (Fig. 13a). In addition, low-frequency variance in the LR04 $\delta^{18}O$ stack that first appeared at 1250 ka remerges 900 ka following a ~100-kyr lull, with renewed power subsequently increasing and remaining as a persistent feature for the remainder of the Pleistocene (Fig. 2, Fig. 13a).

Changes in other components of the climate system at 900 ka suggest possible feedbacks with ice sheets that influenced the subsequent evolution of Pleistocene climate change. Proxies of the Asian monsoon suggest that aridity and wind strength increased and temperatures decreased during this event (Fig. 8). SSTs in the North Atlantic and upwelling regions of the ocean not only completed a long cooling trend that began with the onset of the MPT, but in some cases also reached their lowest values of the MPT at 900 ka (Fig. 13c–13e). Moreover, these SST records exhibit the subdued character of isotope stage 23 as seen in the LR04 stack of ice volume. Meanwhile, interglacial SSTs in the Southern Ocean began to warm at 900 ka (Fig. 5d), suggesting a southward shift of polar fronts and possibly a decrease in the extent of sea ice at these times. Finally, whereas the low-frequency component of North Atlantic SSTs and African and Asian climates emerged at the same time as the onset of the MPT, low-frequency variability only appeared in Pacific SST records at 900 ka (Figs. 7, 9).
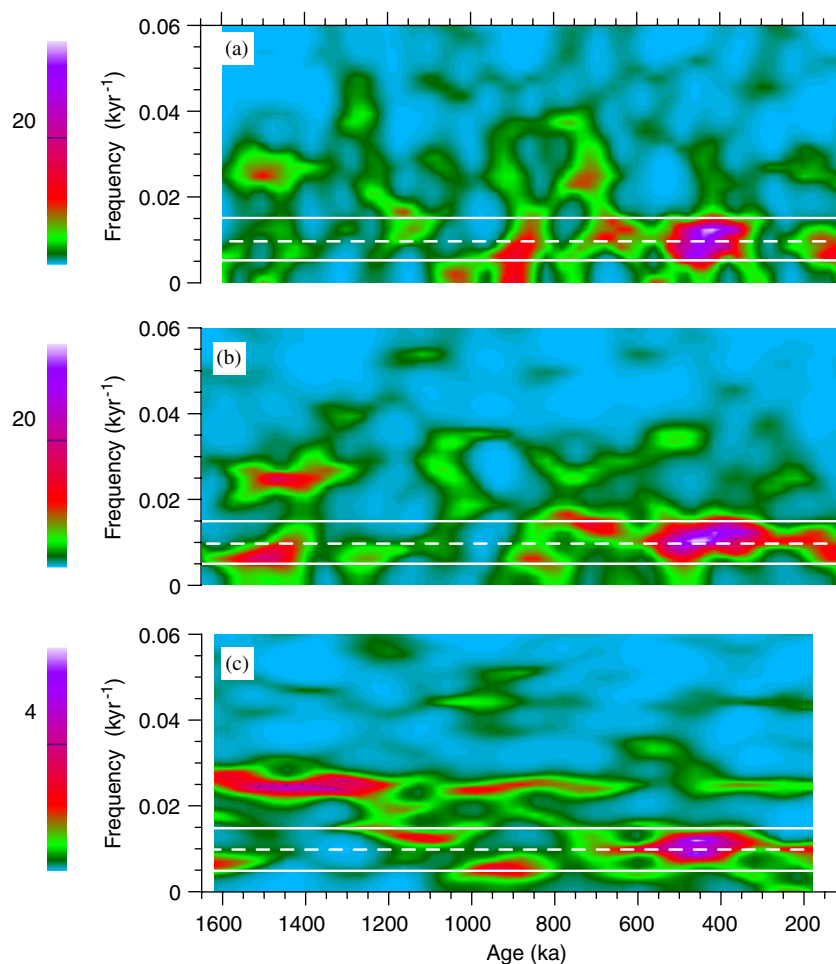
Fig. 12. Time-frequency spectrograms (moving window Fourier transform) showing the distribution of signal power (cycles/kyr) in $\delta^{13}C$ records. Relative power shown by color bars. All time series were detrended, tapered, and filtered forwards and backwards to minimize any phase shift due to the filter. (a) Spectrogram of $\delta^{13}C$ record from DSDP Site 607 (Raymo et al., 1990, with age model transferred to the LR04 stack by M. Raymo, personal communication) (window length = 300 kyr, sliding window length = 30 kyr, high-pass filter with corner frequency 0.00125), (b) Spectrogram of $\delta^{13}C$ record from ODP Site 1090 (Hodell et al., 2003) (window length = 250 kyr, sliding window length = 25 kyr, data interpolated at 0.5 kyr, high-pass filter with corner frequency 0.002), (c) Spectrogram of $\delta^{13}C$ record from ODP Site 849 (Mix et al., 1995a,b) (window length = 350 kyr, sliding window length = 35 kyr, data interpolated at 1.0 kyr, high-pass filter with corner frequency 0.0025). All records are shown on their published age models.

Significant changes in deep-ocean circulation occurred at 900 ka. In particular, $\delta^{13}C$ values in North Atlantic and subAntarctic deep-water records become very depleted (Raymo et al., 1997; Hodell et al., 2003) (Figs. 10a, 13f, h, and $\delta^{13}C$ values in the Pacific reach their most depleted values of the entire 5-Myr long record (Fig. 13g) (Mix et al., 1995b). Clearly this change was global, and requires a significant change in the global partitioning of organic and inorganic carbon.

Following principles established by Shackleton (1977), Raymo et al. (1997) characterized the Pacific and North Atlantic anomalies as a 600-kyr perturbation beginning ~1000 ka induced by the transfer of ^{12}C-enriched terrestrial carbon. We believe the data are more consistent, however, with an event corresponding to isotope stages 24, 23, and 22. Moreover, although Asian proxy records indicate increased aridity at this time, other intervals of similar increased aridity occur without corresponding changes in ocean $\delta^{13}C$ values. So we doubt that episodes of global

aridity were responsible for a transfer of carbon from land to sea. Perhaps the transfer of organic matter came from the erosion of organic-rich soils by the growing ice sheets. But if so, it is difficult to understand why carbon transfer would occur as such an abrupt event when the area of the ice sheets was similar before and after the MPT. Further, oxidation of this soil carbon would likely imply an increase in atmospheric pCO_2 (Broecker, 1982), which unless counteracted by other effects would seem inconsistent with observations of abrupt cooling at that time.

An alternative scenario may be that the transfer of organic matter into the DIC in the ocean during the 900-kyr event came from continental shelf and slope deposits. The rapid increase in ice-sheet thickness (and thus ice volumes) during glaciation events during this time interval (e.g., Kitamura and Kawagoe, 2006) would have dropped sea levels lower than they had been for millions of years, potentially exposing rich accumulations of marine organic matter to oxidation within the marine system. As noted by
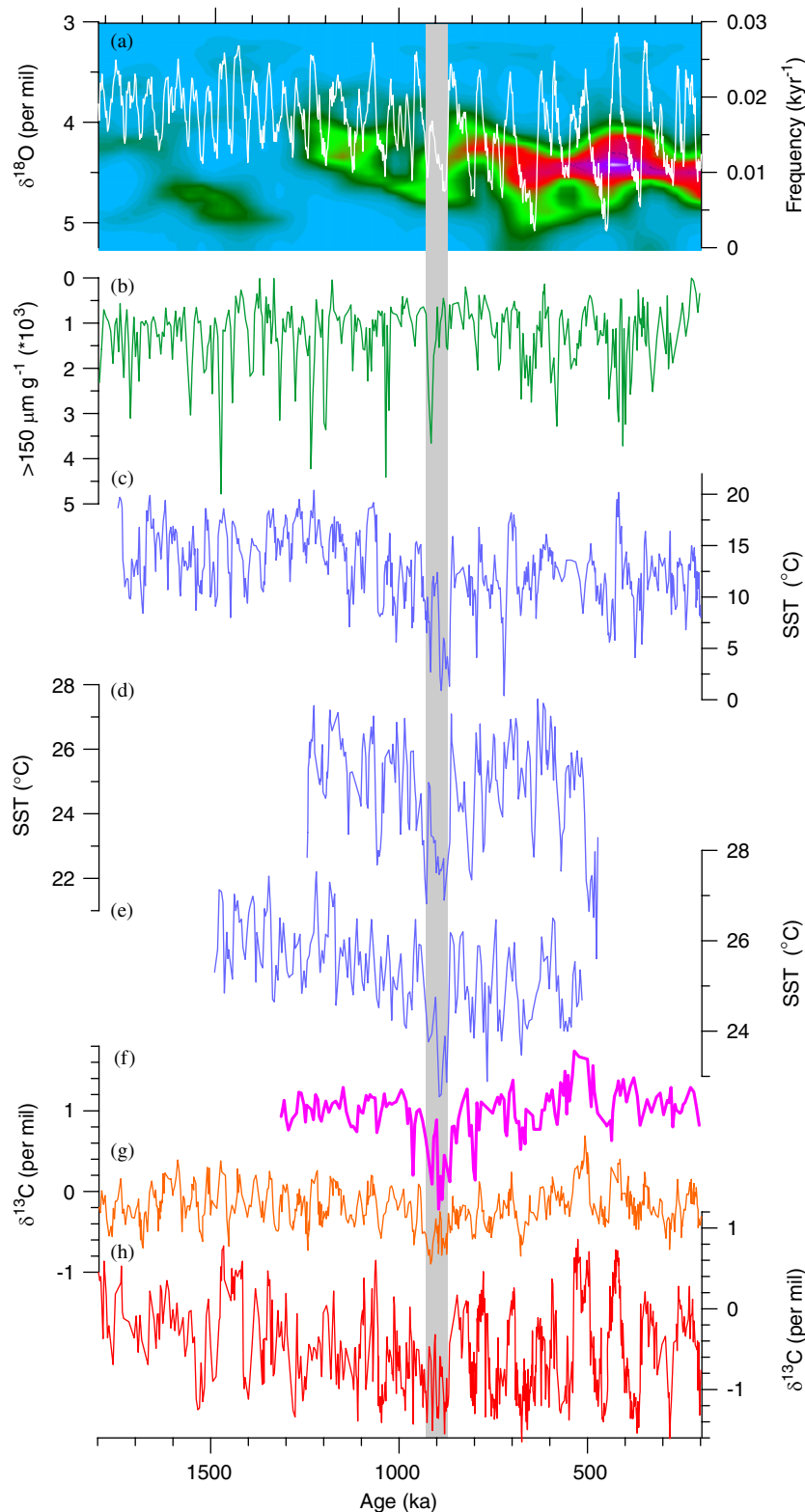
Fig. 13. Climate records showing evidence of a notable climate excursion at 900 ka. (a) Time-frequency spectrogram (moving window Fourier transform) showing the distribution of low-frequency power in the 100-kyr filtered LR04 $\delta^{18}O_b$ stack (cycles/kyr) (window length 350 kyr, sliding window length 35 kyr, high-pass filter = 0.00125, low-pass filter = 0.025). Superimposed on spectrogram (in white) is the LR04 $\delta^{18}O_b$ stack (Lisiecki and Raymo, 2005), (b) Record of ice-rafted debris into the Norwegian Sea (Jansen et al., 2000), (c) North Atlantic SSTs from DSDP Site 607 based on census counts of foraminifera (Ruddiman et al., 1989), (d) Alkenone record of eastern tropical Atlantic SSTs off the west coast of Africa (ODP Site 1077) (Schefus et al., 2004), (e) Alkenone record of SSTs from the eastern equatorial Pacific (ODP Site 849) (McClymont and Rossel-Mele, 2005), (f) $\delta^{13}C$ record measured on *Cibicidoides wuellerstorfi* from North Atlantic DSDP Site 552 (56°N) (Raymo et al., 1990), (g) $\delta^{13}C$ record from ODP Site 849 (Mix et al., 1995a,b), (h) $\delta^{13}C$ record from ODP Site 1090 (Hodell et al., 2003). All records are shown on their published age models.

Broecker (1982), such a mechanism would shift deep-sea $\delta^{13}C$ values without causing an associated rise in atmospheric CO_2 (and perhaps even causing a fall in CO_2, depending on the ratio of nutrients to carbon transferred). By the end of the MPT, sea levels had reached lowstands comparable to those associated with the rest of the late Pleistocene, suggesting an end to the anomalous transfer of organic matter into the ocean from the shelves, and a gradual relaxation of oceanic $\delta^{13}C$ back toward its long-term equilibrium at higher values. This would occur with a time constant of several hundred thousand years, the residence time of carbon in the ocean (Mix et al., 1995a).

5. Mechanisms to cause the MPT

The enigma of the MPT is that it involved the emergence of ~100-kyr cycles in the absence of any obvious change in the orbital forcing. Fig. 14 illustrates this point by showing that while the amplitude of the 100-kyr signal is increasing in the LR04 stack (Fig. 14d), the amplitude of the 100-kyr signal in insolation decreases (Fig. 14c). Moreover, the essence of the "100-kyr cycle problem" is that while the dominant ice-volume cycle of the last 700 ka is at the 100-kyr frequency (Fig. 14f), there is virtually no corresponding power in insolation forcing (Fig. 14e). These observations suggest that any explanation for the emergence and dominance of the 100-kyr climate cycle must also include the physics that prevented the 100-kyr cycle from occurring prior to 1250 ka.

Most hypotheses for the MPT invoke some change internal to the climate system in response to a long-term cooling (Oerlemans, 1984; Saltzman and Maasch, 1991; Raymo, 1997; Mudelsee and Schulz, 1997; Paillard, 1998; Berger et al., 1999; Tziperman and Gildor, 2003; Rial, 2004). The cause of the cooling itself is often attributed to an assumed secular decrease in atmospheric pCO_2 (e.g., Raymo, 1997; Mudelsee and Schulz, 1997; Paillard, 1998; Berger et al., 1999). This explanation for the MPT tacitly assumes a known climate sensitivity to atmospheric pCO_2 in order to induce a response at precisely the time of the MPT. Moreover, the EPICA ice core, which provides the longest available record of atmospheric pCO_2 (Siegenthaler et al., 2005), indicates that mean atmospheric pCO_2 was lower at 720 ka (~230 ppmV) than today (~240 ppmV). Accordingly, if a secular decrease in atmospheric pCO_2 ultimately caused the MPT, that trend had reversed by at least 720 ka.

Regardless of its cause, a number of models demonstrate that a gradual cooling would be a viable candidate for causing the MPT, although its manifestation may occur through one of several possible system responses to that cooling. Berger et al. (1999), for example, modeled ice-sheet response to insolation forcing. Under a warmer climate induced by higher atmospheric pCO_2, ice sheets never grow large enough during insolation minima to survive any subsequent moderate insolation maxima, resulting in 41-kyr cycles. In contrast, a decrease in atmospheric pCO_2 with an attendant cooler climate allows ice sheets to survive through moderate insolation maxima, and only deglaciate entirely under maximum insolation forcing (high eccentricity, high obliquity, boreal summer at perihelion).

Tziperman and Gildor (2003) proposed that long-term deep-water cooling of unspecified cause induced the MPT. The key process involved in their model is the effect of sea-ice on ice-sheet mass balance: large sea-ice cover induces a more negative mass balance by cooling the atmosphere, diverting storm tracks, and reducing evaporation from the subpolar oceans. According to Tziperman and Gildor, sea-ice cover is linked to deep-water temperature. Warmer deep-water reduces the density difference between the deep-ocean and the surface ocean, thus enhancing vertical mixing. The resulting density contrast increases the heat capacity of the combined system (relative to the surface ocean) and enhances thermohaline circulation, further linking the surface and deep-oceans. For a given atmospheric cooling, the effect of the warm deep-ocean thus inhibits sea-ice expansion until very cold atmospheric temperatures are achieved. In contrast, the effect of a cold deep-ocean is to limit the heat capacity of the surface ocean, allowing sea ice to form at warmer atmospheric temperatures than for a warm deep-ocean. In both cases, sea-ice growth occurs rapidly through the ice-albedo feedback, but the differing temperatures at which sea-ice forms affects ice-sheet mass balance response to temperature differently. For warm deep-water, ice-sheet mass balance varies linearly with temperature, causing smaller symmetrical oscillations in ice volume. For cold deep-water, the effect of rapid sea-ice growth is to starve ice sheets of moisture, introducing larger asymmetrical oscillations in ice volume.

Rial (2004) described the MPT as a simple case of the climate system transforming amplitude modulation into frequency modulation. For instance, Rial used a simplified nonlinear climate model to show that a step-like drop in global mean temperature can increase the period of oscillation drastically, from 41 to 95 kyr. Physically, a step-like drop in temperature changes the carrying capacity of the system, which controls the size of ice sheets. A slightly colder world allows for greater ice-sheet extent, and as long as the temperature is maintained at the lower level, the longer period will persist and its amplitude will be greater than that of the previous cycle. For this to happen, the climate system is assumed to freely oscillate at periods close to (within ~15%) the Milankovitch forcing. This allows entrainment to occur, as the 41 and 95 kyr periods of the forcing synchronize with the free oscillations of the climate, whose periods are of course unknown. The process is analogous to the synchronization of a circadian biological clock (the analogue of the climate oscillator) to the 24-h day cycle forcing (e.g., Pikovsky et al., 2001). If the analogy is correct, the spectrum of the climate system has peak responses at periods near to (but not necessarily identical to) those of the astronomical forcing. Evidence
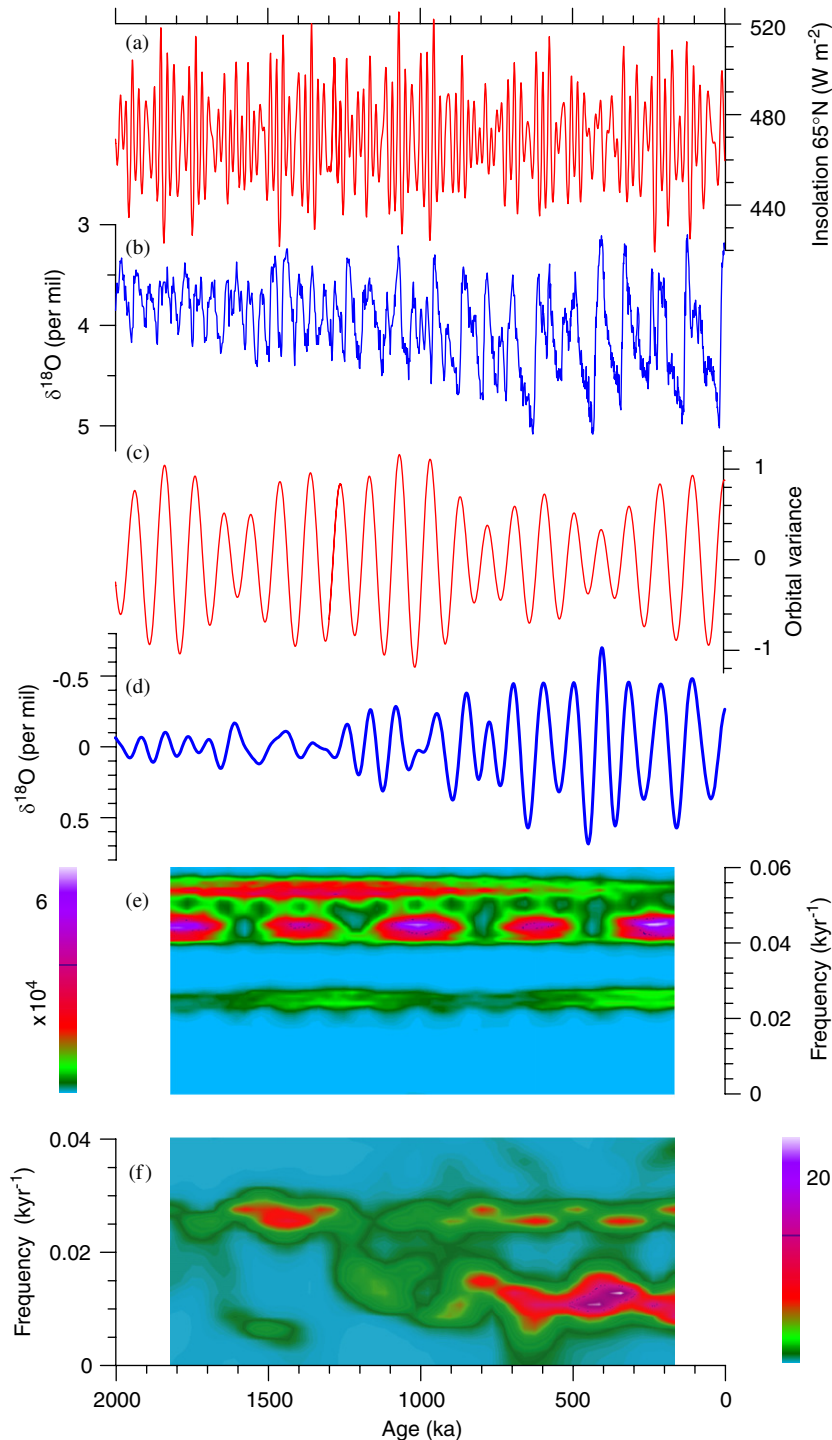
Fig. 14. (a) June-July insolation at 65°N (Laskar et al., 1993), (b) The LR04 $\delta^{18}O$ stack (Lisiecki and Raymo, 2005), (c) Filtered July 65°N insolation using a 100-kyr filter, (d) Filtered LR04 stack using a 100-kyr filter, (e) Time-frequency spectrogram (moving window Fourier transform) showing the distribution of signal power (cycles/kyr) in July 65°N insolation (window length = 300 kyr, sliding window length = 30 kyr, no filter, not detrended), (f) Time-frequency spectrogram (moving window Fourier transform) showing the distribution of signal power (cycles/kyr) in LR04 $\delta^{18}O$ stack (window length = 350 kyr, sliding window length = 35 kyr, detrended, tapered, and filtered forwards and backwards to minimize any phase shift due to the filter, high-pass filter with corner frequency 0.0012).

from tropical temperatures (especially the tropical Pacific) reviewed here, and evidence from biogenic sedimentation in the eastern Pacific shows that long-period variations in the climate system with periods near 100 kyr existed prior to the MPT, and Mix et al. (1995a) note the apparent

entrainment effect (as a discrete phase shift of the 100-kyr cycle) during the MPT, so this mechanism has merit.

A step-like drop in insolation amplitude did occur around 1000 ka (Fig. 14a), but its timing is younger than the beginning of the MPT at ~1250 ka, suggesting that the

Rial (2004) mechanism cannot be the only cause of the MPT; some other mechanism must have triggered the change in regime. The presence in the LR04 stack of a ~100-kyr lull in 100-kyr power centered on 1000 ka (Fig. 2e, f) may suggest an aborted attempt to initiate 100-kyr glaciations that was kick-started again by additional cooling induced by the decrease in insolation amplitude. The LR04 stack also shows a small but significant increase in mean interglacial $\delta^{18}O_b$ from ~1000 ka until 700 ka, followed by a decrease at 400 ka (Fig. 14b), corresponding to a decrease and then increase in insolation amplitude (Fig. 13a, 14c), thus also suggesting a possible insolation influence on long-term ice-sheet evolution. We note, however, that earlier decreases in the amplitude of insolation forcing do not correspond to growth of 100-kyr climate cycles, further suggesting that any associated climate influence may simply have reinforced ongoing mechanisms involved in causing the MPT.

6. The regolith hypothesis

Models demonstrate several physically reasonable mechanisms by which a gradual decrease in temperature may induce an increase in ice volume with a corresponding change in frequency. The associated increase in ice volume is either represented by an increase in ice area as a proxy for volume (Tziperman and Gildor, 2003; Rial, 2004) or is computed directly (Berger et al., 1999), with area assumed either implicitly or explicitly to scale with volume

$$V = c\pi A,$$

where c is a proportionality constant that reflects controls on ice flow (Paterson, 1972). In doing so, these models predict smaller-area pre-MPT ice sheets than post-MPT ice sheets, and thus fail to account for the evidence that the earliest Northern Hemisphere ice sheets covered a similar or larger area than those that followed the MPT (Fig. 15). Given that the MPT was associated with an increase in ice volume (Fig. 3), the existence of late Pliocene and early Pleistocene ice sheets that were as extensive as during the late Pleistocene requires an increase in ice thickness to explain the increase in ice volume, and thus that the controls on ice flow that set the scaling relation between area and volume must have changed.

Clark and Pollard (1998) attributed the change in ice flow to the gradual removal by ice-sheet erosion of a thick regolith to eventually expose unweathered crystalline bedrock, with an attendant change from a low-friction substrate provided by the regolith to a high-friction substrate provided by the crystalline bedrock. The presence of a former regolith mantling the crystalline shields that underlie the central core regions of former Northern Hemisphere ice sheets (Clark et al., 1999) is an expected outcome of the 10^7–10^8 yr that the shield bedrock was exposed to weathering prior to the onset of Northern Hemisphere glaciation. Following the onset of Northern Hemisphere glaciation, the low-friction regolith thus

favored the development of thin but areally extensive ice sheets that responded linearly to the 41-kyr insolation forcing. Successive glaciations eventually gave rise to the MPT through the subglacial erosion of the regolith and consequent unroofing of unweathered crystalline bedrock, with the resultant high-friction substrate inducing thicker ice sheets with a fundamentally different response to the insolation forcing.

To test this hypothesis, Clark and Pollard (1998) used a physical ice-sheet/sediment model that predicts Laurentide ice-sheet thickness, sediment thickness and bedrock elevation versus latitude and time, in a 1-D transect running north–south from the Arctic basin to the mid-latitudes of central North America. The ice sheet uses a standard shallow-ice flow law, and is forced by a prescribed pattern of surface accumulation minus ablation shifted vertically to represent Milankovitch orbital variations. Calving by proglacial lakes or marine incursions is invoked whenever the southern ice-sheet margin falls below sea level, which is important in producing complete deglaciations and 100-kyr cycles after the MPT. The depression and rebound of bedrock elevation under the ice load is simply a local relaxation towards isostatic equilibrium with a 5000-year time lag.

Thickness of regolith is initialized at the start of each run (3 Ma) to a uniform 50 m, representing the regolith produced by pre-glacial weathering. When overlain by ice, regolith is deformed and transported horizontally by the basal ice-sheet shear stress, assuming a weakly nonlinear till rheology (Boulton and Hindmarsh, 1987; Jenson et al., 1996). A maximum limit of 500 m is imposed on sediment thickness in ice-free areas, crudely mimicking riverine transport. This version of the model neglects generation of new till by the action of ice on bedrock, so all sediment originates from the initial regolith layer. Subglacial sediment deformation has an important effect on ice dynamics, causing extra basal sliding that keeps ice-sheet profiles relatively thin and resulting in dominant 20- and 40-kyr cyclicity before the MPT; after the MPT, much of the sediment has been eroded and the ice sheets rest on hard bedrock, producing steeper and thicker ice-sheet profiles and allowing dominant nonlinear 100 kyr cyclic behavior (Fig. 16).

Several lines of evidence support the presence of a former regolith as well as its subsequent erosion by the Laurentide Ice Sheet at the time of the MPT. Direct evidence of this regolith comes from central and western Minnesota, where a deep saprolite, averaging 30 m in thickness but with local thickness >60 m, is developed in Precambrian crystalline bedrock (Goldich, 1938; Setterholm and Morey, 1995). Similar, though less extensive, pre-Quaternary saprolites preserved on glaciated crystalline bedrock also occur in eastern Canada (Wang et al., 1981; McKeague et al., 1983). In contrast, thick saprolites continuously mantle metamorphic terrain in the Appalachian Mountains south of the glacial border (Mills and Delcourt, 1991), pointing to a distinct boundary in regolith distribution determined by glacial erosion.
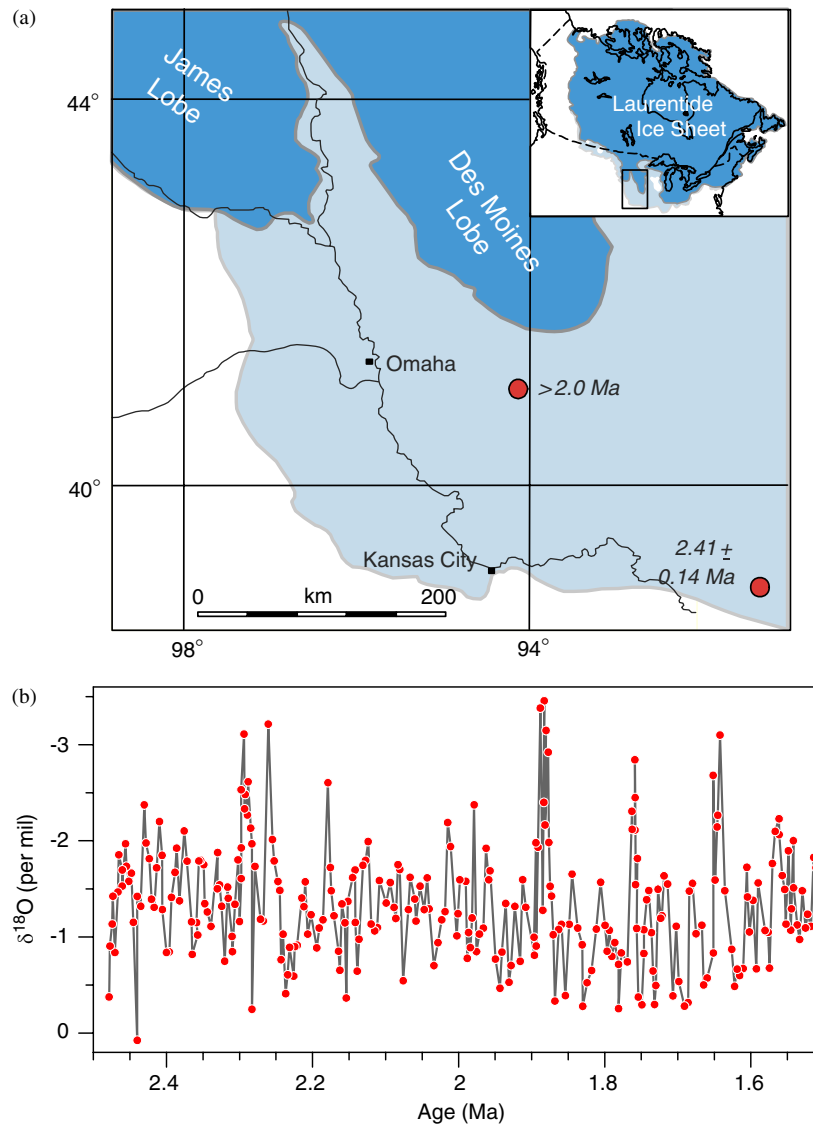
Fig. 15. (a) Maximum limit of Laurentide Ice Sheet in the North American midcontinent (light blue area) showing a greater areal extent relative to the limit reached by the ice sheet during the last glacial maximum 21 ka (LGM) (dark blue area). Till deposited by the Laurentide Ice Sheet in Iowa is overlain by the 2.0-Ma Huckleberry Ridge Ash derived from the Yellowstone caldera (Boellstorf, 1978; Roy et al., 2004a). Other tills suggest multiple advances of the LIS into this region between 0.8 and 2.0 Ma (Roy et al., 2004a). Balco et al. (2005) dated a till in Missouri using ^{10}Be/^{26}Al at 2.41 ± 0.14 Ma, (b) Further support for extensive advances of the LIS margin into the midcontinent during the late Pliocene and early Pleistocene comes from a planktic δ^{18}O record from the Gulf of Mexico, which suggests that the southern LIS margin repeatedly entered the Mississippi River drainage after 2.3 Ma and discharged light δ^{18}O meltwater to the Gulf of Mexico (Joyce et al., 1993), similar to meltwater events that occurred during the last deglaciation (Kennett and Shackleton, 1975).

Evidence for sufficient erosion of the regolith to begin exposing crystalline bedrock at the start of the MPT is registered in terrestrial and marine records. Because chemical weathering involves the removal of the more reactive mineral species, resulting in a composition that reflects the more resistant minerals as well as the products of chemical weathering of the more reactive species, sediments derived from regolith will have a different mineralogical and geochemical signature than sediments derived from fresh crystalline bedrock. Such a distinction is seen in tills from the North American mid-continent, where Boellstorf (1978) first noted that the oldest (unweathered)

tills (>2 Ma) are enriched in stable minerals and weathered products and depleted in unstable minerals compared to younger tills. Roy et al. (2004a, b) found similar first-order mineralogical changes as well as geochemical changes in the silicate fraction of midcontinent tills that further indicated a temporal change from a regolith to an unweathered bedrock source. In refining the till stratigraphy of the midcontinent, Roy et al. (2004b) established that enrichment of the tills in minerals and major elements indicative of an unweathered bedrock source occurred during the early and middle Pleistocene, and that tills deposited during the Brunhes Chron (<780 ka) show
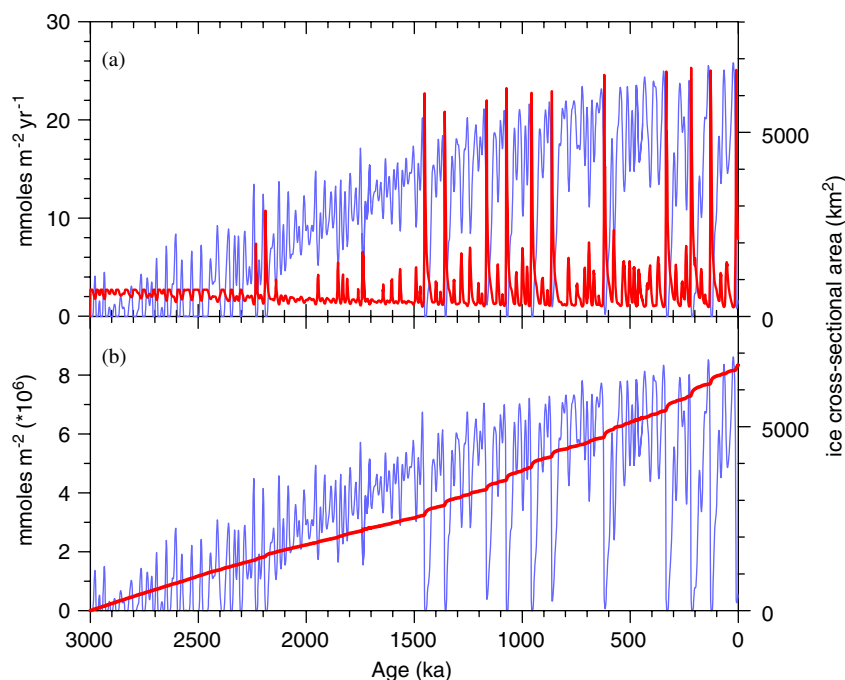
Fig. 16. (a) Blue curve: Ice-sheet cross-sectional area in a North American ice sheet-sediment flowline model, driven by orbital insolation perturbations over the last 3 million years (nominal simulation in Clark and Pollard, 1998). Red curve: Instantaneous weathering rate over the model domain (see text), (b) As in (a) except the red curve shows accumulated weathering averaged over the model domain, i.e., the time integral of the instantaneous curve from the start of the run.

major-element concentrations that are most similar to that of fresh shield bedrock.

Additional mineralogical evidence for a change from a regolith to unweathered bedrock source during the middle Pleistocene comes from ODP Site 645 in Baffin Bay, which records a direct influence of the adjacent Laurentide and Greenland ice sheets beginning with the first ice rafting in the Pliocene (Thiebault et al., 1989). In particular, Andrews (1993) distinguished three units on the basis of changes in clay-size mineralogy: a unit deposited 2000–1200 ka characterized by smectite and no calcite, a unit deposited 1200–500 ka characterized by kaolinite and the first appearance of calcite, and a unit deposited 500–0 ka characterized by dolomite. Thiebault et al. (1989) also described a change at 950 ka from clay minerals derived from weathered bedrock (smectites) to those derived from unweathered crystalline bedrock (chlorite and illite).

Three marine tracers of continental weathering provide further support for the exhumation of fresh silicate bedrock during the MPT. The record of $^{87}Sr/^{86}Sr$ of dissolved Sr in seawater reflects a balance between contributions from hydrothermal sources at midocean ridges, marine diagenesis, and chemical weathering of continental rocks. On timescales of interest here, we can consider the first two sources as constant, so any change in marine $^{87}Sr/^{86}Sr$ must reflect changes in the continental source, which is determined by the flux of Sr to the ocean and its $^{87}Sr/^{86}Sr$ value. The specific mechanisms driving the general increase in seawater $^{87}Sr/^{86}Sr$ during the Cenozoic

are still a subject of debate, but the primary ones are thought to involve uplift-induced weathering of lithologies in the Himalayan region with high $^{87}Sr/^{86}Sr$ (Raymo et al., 1988; Richter et al., 1992; Derry and France-Lanord, 1996) and glaciation (Armstrong, 1971; Hodell et al., 1989; Capo and DePaolo, 1990; Farrell et al., 1995; Blum and Erel, 1995).

Based on the observation by Blum and Erel (1995) of a negative correlation between ^{87}Sr and ^{86}Sr of exchangeable Sr in soils developed in silicate minerals and the soil age, the regolith hypothesis makes a distinct prediction as to how the marine $^{87}Sr/^{86}Sr$ record would evolve following the onset of Northern Hemisphere glaciation. An initial increase in seawater $^{87}Sr/^{86}Sr$ would correspond to the increased flux of Sr from the continents with relatively low $^{87}Sr/^{86}Sr$ values reflecting a regolith source. Exposure of fresh silicate rocks would increase the $^{87}Sr/^{86}Sr$ value of the continental Sr flux, and thus accelerate the increase in seawater $^{87}Sr/^{86}Sr$.

The evolution of marine $^{87}Sr/^{86}Sr$ over the last 5 Ma shows the apparent effect of the onset of Northern Hemisphere glaciation in causing seawater $^{87}Sr/^{86}Sr$ to increase at 2800 ka at a rate of $\sim 0.3 \ 10^{-10} \, yr^{-1}$ (Fig. 17c) (Farrell et al., 1995). In support of the regolith hypothesis, however, the rate of increase in seawater $^{87}Sr/^{86}Sr$ then accelerates at ~ 1400 ka to $\sim 0.5 \ 10^{-10} \, yr^{-1}$, or at a rate similar to that modeled by Blum and Erel (1995) when accounting for weathering of freshly exposed silicate minerals on 100-kyr glacial timescales. Given the scatter
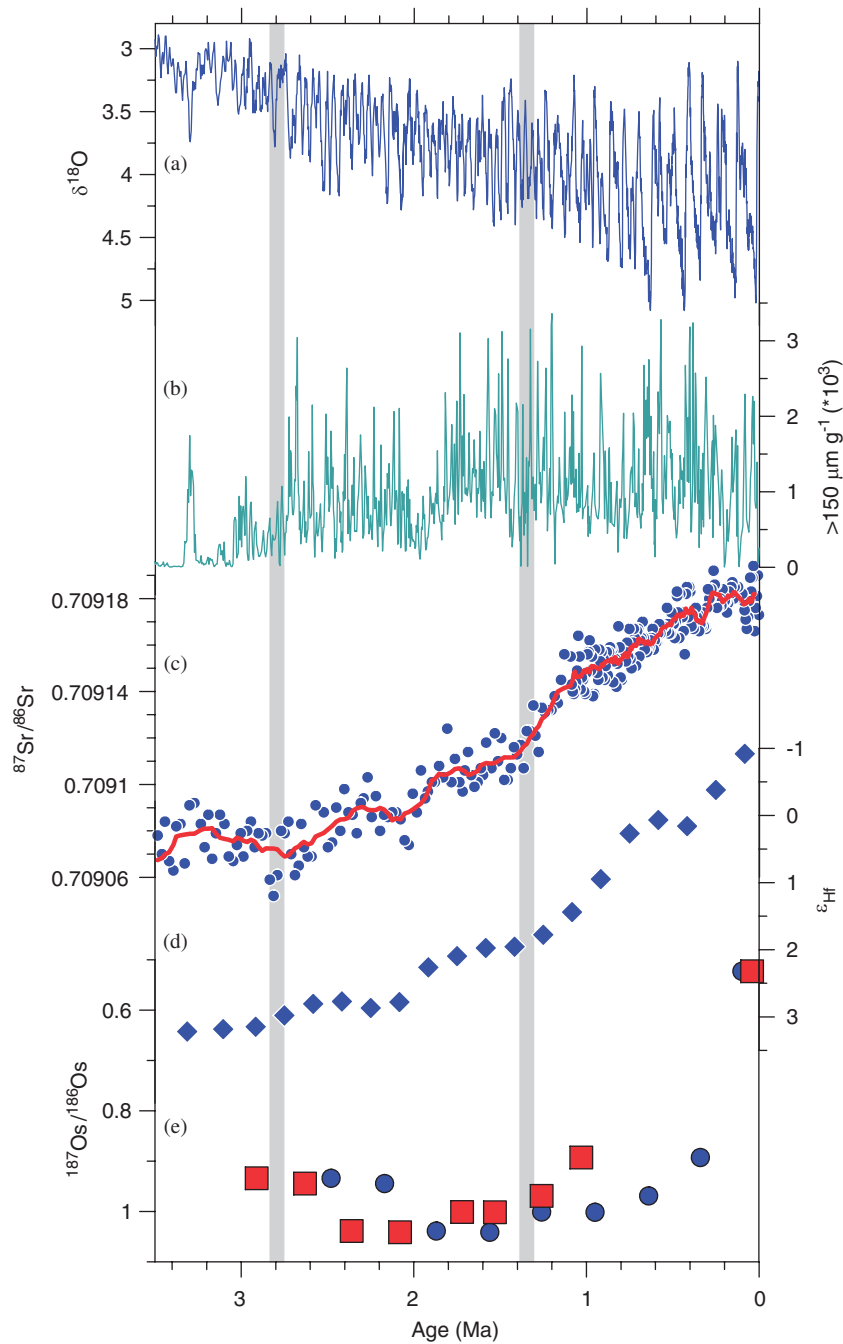
Fig. 17. (a) The LR04 $\delta^{18}O$ stack (Lisiecki and Raymo, 2005), (b) Record of ice-rafted debris into the Norwegian Sea (Jansen et al., 2000), (c) Record of seawater $^{87}Sr/^{86}Sr$ from DSDP Site 758 (Farrell et al., 1995), (d) Record of ε_{Hf} in seawater from NW Atlantic ferromanganese crusts (van der Flierdt et al., 2002), (e) Record of $^{187}Os/^{186}Os$ from central Pacific ferromanganese crusts (Burton et al., 1999). Age model for red data is based on Th ages, whereas age model for blue data is based on Be ages. The two narrow gray vertical bars identify times of excursions in weathering proxies. All records are shown on their published age models.

in the marine Sr isotope record, determining the exact time of this acceleration in the increase of seawater $^{87}Sr/^{86}Sr$ is difficult. However, it does appear to precede the emergence of the 100-kyr climate cycle by perhaps 150 kyr, suggesting that sufficient unweathered silicate bedrock initially became exposed to contribute radiogenic Sr, but another 150,000 years (three 41-kyr glacial cycles) were required to

expose the area of hard bedrock needed to affect ice-sheet size and attendant response.

A record of ε_{Hf} in seawater from NW Atlantic ferromanganese crusts also indicates changes associated with the onset of Northern Hemisphere glaciation (van der Flierdt et al., 2002) (Fig. 17d). In this case, the overall decrease in ε_{Hf} values at ~2800 ka is attributed to an

increase in glacial crushing and partial dissolution of zircons, which are the primary reservoir of unradiogenic Hf (van der Flierdt et al., 2002). Of significance here, however, is the fact that the rate of decrease in ε_{Hf} values accelerated beginning ~1200 ka, at which point the rate of decrease remained constant to the present (Fig. 17d). We suggest that this latter trajectory of ε_{Hf} values may reflect enhanced crushing of minerals in response to increasing surface area of exposed Canadian Shield bedrock caused by progressive erosion of regolith. Exposure of hard bedrock at the ice-bed interface would induce greater rates of mineral crushing relative to that associated with a soft, regolith-floored substrate (Cuffey and Alley, 1996). Rates of mineral crushing would then remain constant when the entire shield became exposed, thus delivering a constant and high flux of unradiogenic Hf to the ocean.

Osmium is another tracer of continental weathering, with higher $^{187}Os/^{186}Os$ ratios indicating an increase in silicate weathering rates (Peucker-Ehrenbrink and Blum, 1999). For example, the slightly more radiogenic nature of North Atlantic seawater compared with other ocean water masses may reflect the enhanced silicate weathering of recently deglaciated shield areas surrounding the North Atlantic Ocean (Peucker-Ehrenbrink and Blum, 1999). Burton et al. (1999) reported a low-resolution $^{187}Os/^{186}Os$ record that showed constant seawater values between 3000 and ~1000 ka, followed by a steep increase in $^{187}Os/^{186}Os$ to the present (Fig. 17e). Unlike Sr isotopes, radiogenic Os in highly weathered soils is strongly depleted relative to the bulk soil fraction so that an increased continental flux of such material would not influence seawater $^{187}Os/^{186}Os$. Accordingly, Peucker-Ehrenbrink and Blum (1999) suggested that the initial period of a constant seawater $^{187}Os/^{186}Os$ reflected regolith erosion by ice sheets, whereas subsequent exposure of unweathered silicate bedrock is reflected by an increase in seawater $^{187}Os/^{186}Os$.

Another potential indicator of increased silicate weathering associated with the MPT is the record of carbonate preservation in the deep sea. Silicate weathering adds alkalinity to the ocean, which is then removed by organisms growing calcite shells. The vertical distribution of $CaCO_3$ in the ocean reflects the concentrations of Ca^{2+} and CO_3^{2-}, which are constant with depth, relative to the increase in calcite solubility with pressure. At some depth, waters become undersaturated with respect to $CaCO_3$ and calcite begins to dissolve; thus the deepest parts of the oceans are largely barren of $CaCO_3$. Because the state of saturation of the ocean is set by the concentrations of Ca^{2+} and CO_3^{2-}, an increase in their flux to the oceans, such as would occur with the exposure of crystalline-shield bedrock, should then be registered by greater preservation of $CaCO_3$ to greater depths.

The possibility that increased alkalinity affected whole-ocean chemistry at the time of the MPT is suggested by the record of $CaCO_3$ preservation in the central equatorial Pacific (Farrell and Prell, 1991) (Fig. 18b). In general, $CaCO_3$ preservation improved at the start of Northern Hemisphere glaciation, but the top of the transition zone (~80% $CaCO_3$) remained largely above 3900 m until ~1500 ka, when it deepened, fluctuating between 4200 and 4400 m on glacial–interglacial timescales and with a pronounced shoaling associated with dissolution during the global mid-Brunhes dissolution cycle (Fig. 18b). At the same time, the bottom of the transition zone (i.e., compensation depth) began to deepen, also with an oscillation during the mid-Brunhes dissolution cycle (Fig. 18b).

7. Long-term silicate weathering rates

Blum and Erel (1995) and Blum (1997) suggested that repeated advances and retreats of Northern Hemisphere ice sheets have been particularly effective in increasing the oceanic $^{87}Sr/^{86}Sr$ ratio. Each advance of the ice-sheets erodes and comminutes more fresh bedrock, which then undergoes chemical weathering when the ice-sheet retreats. Blum and Erel (1995) found that measured $^{87}Sr/^{86}Sr$ in Sr released from granitoid soils is significantly higher in the early stages of weathering, subsequently declining on time scales of several thousand years. Similarly Blum (1997) describes how overall chemical erosion rates decline with time after exposure of fresh bedrock. Thus, the repeated exposure of newly comminuted bedrock by glacial cycles counteracts the decline that would occur with a single glacial episode, and Blum and Erel (1995) used their soil data to quantitatively estimate the enhanced increase of oceanic $^{87}Sr/^{86}Sr$ due to repeated 100-kyr glacial cycles.

Here we extend their calculation using the ice-sheet and regolith model previously used to simulate variations of the Laurentide ice sheet over the last 3 Myr (Clark and Pollard, 1998). Because the model successfully captures the MPT (i.e., ~20 and 40-kyr cyclicity in ice volume transitioning to dominant larger-amplitude ~100-kyr cycles) (Fig. 16), we can test if changes in the character of glaciation across the MPT affect long-term weathering fluxes, and if there is any correspondence with the record of seawater $^{87}Sr/^{86}Sr$ described above.

To include chemical weathering and $^{87}Sr/^{86}Sr$ fluxes, we simply prescribe chemical weathering of exposed regolith or bedrock at each grid point, allowing for the elapsed time that sediment-free bedrock has been exposed since last overlain by ice (T_{expose}). At each model time step and grid point, the following steps are performed:

1. For ice-covered grid points, there is no chemical erosion. If there is no regolith, then fresh bedrock is being comminuted (quarried or abraded) by the basal ice, so T_{expose} is reset to zero.
2. For ice-free grid points:
   a. If regolith is present, the bedrock is covered so there is no weathering of bedrock. But regolith is chemically weathered at the relatively slow rate of 2.7 mmol m^{-2} yr^{-1} (of Ca + Mg, the weathering of
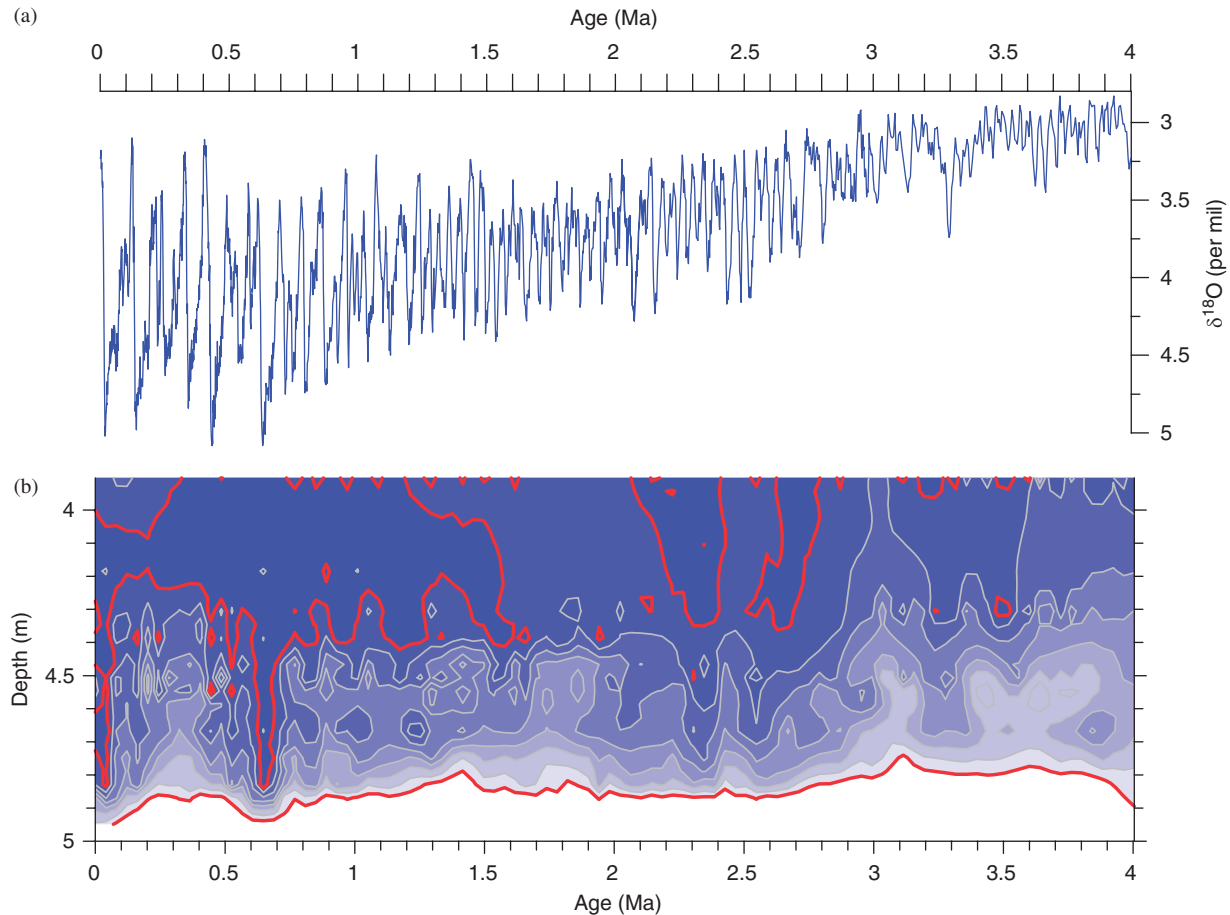
Fig. 18. (a) The LR04 $\delta^{18}O$ stack (Lisiecki and Raymo, 2005), (b) Contoured plot of percent carbonate from the equatorial Pacific Ocean as a function of depth and time (data from Farrell and Prell, 1991). Contour interval is 10%, with deeper red contour equal to 10% and shallower red contour equal to 80%.

which consumes atmospheric CO_2; e.g., Berner, 2004).

b. If no regolith is present, chemical erosion of bedrock occurs at a rate $72 \, (T_{expose}/1000)^{-0.71} \, \mathrm{mmol \, m^{-2} \, yr^{-1}}$, following the power law relationship defined by Blum (1997), Eq. (9) and supported by White and Brantley (2003) but modified to coincide with measurements of modern day silicate weathering rates determined by chemical fluxes from large river systems of the Canadian Shield (Millot et al., 2002). For T_{expose} less than 1000-years-old, a maximum value of $72 \, \mathrm{mmol \, m^{-2} \, yr^{-1}}$ corresponding to a 1000-year surface age is adopted. T_{expose} is incremented by the model timestep in years.

Results are shown in Fig. 16. The thin blue line in each panel shows ice-sheet cross-sectional area, identical to the nominal simulation in Clark and Pollard (1998) (which is unaffected by the chemical weathering parameterizations). As discussed above, smaller higher-frequency variations dominate before the modeled "MPT" (occurring here at 1500 ka) and larger ~100 kyr variations dominate afterwards. The thick red curve in Fig. 16A shows the

instantaneous chemical weathering, averaged over the model domain (75–40°N). The low "background" value is due to erosion of regolith, and spikes occur when ice extent recedes after an advance, exposing freshly comminuted bedrock. These spikes become much larger after the MPT, when more bedrock area is regolith-free and ice advances further southward during glaciations.

The thick red curve in Fig. 16b shows accumulated weathering, i.e., the time integral of the instantaneous weathering from the start of the run. We take this to be proportional to the flux of silicate-derived Sr to the oceans due to Northern Hemispheric glaciations. Recall that younger weathering surfaces should also yield higher $^{87}Sr/^{86}Sr$ of this flux. The rate of increase accelerates markedly at ~1500 ka with the onset of large ~100-kyr variations, since (i) each major deglaciation produces a very large spike in chemical weathering, and (ii) in between the major deglaciations, the 20- and 40-kyr cycles (due to direct orbital forcing) produce minor chemical weathering spikes similar to or slightly larger than before 1500 ka. We note that the modeled increase in slope at 1500 ka coincides with the timing of the observed increase in slope in the $^{87}Sr/^{86}Sr$ record. Due to the ~2-Myr residence time of Sr in

the oceans, changes in marine $^{87}Sr/^{86}Sr$ resulting from changing inputs would be highly damped compared to the input function (e.g., Blum, 1997).

8. Carbon cycle modeling

8.1. Model formulation

8.1.1. Silicate weathering and CO_2

The carbon cycle model is driven by CO_2 input from the earth to the atmosphere, considered to be constant at a rate of 6×10^{12} mol yr^{-1}, consistent with the model of Berner (2004) and within his cited observational range of $4–10 \times 10^{12}$ mol yr^{-1}. CO_2 is consumed by silicate weathering, following the formulation:

$$CO_2 \text{ uptake} = 6 \times 10^{12} \text{ mol/yr } F_{BT}(CO_2)F_{shield}.$$

The factors $F_{BT}(CO_2)$ and F_{shield} are unitless, nominally equal to 1.0 under standard conditions so that the rate of CO_2 uptake would balance degassing (6×10^{12} mol/yr). The factor $F_{BT}(CO_2)$ represents the effect of atmospheric CO_2 on silicate weathering rates. Its parameterization is based on Berner (2004) and Berner and Kothavala (2001) to be

$$F_{BT}(CO_2) = \left(R_{CO_2}\right)^{Z \cdot \Gamma}\left(1 + RUN \, \Gamma \, \ln\left(R_{CO_2}\right)\right)^{0.65}.$$

Atmospheric CO_2 is described by R_{CO_2} defined as pCO$_2$/280. The first factor on the right-hand side of the equation is an increase in the reaction rate from increased temperature. The activation energy, Z, is set to a value 0.09. Γ is Berner's nomenclature for the climate sensitivity, ΔT_{2x}. We use $3\,°C$, while Berner and Kothavala (2001) use $4\,°C$ in their standard run. The second factor on the right describes the effect of changing runoff on weathering. The variable RUN describes the sensitivity of runoff to temperature, d runoff/dT. Berner and Kothavala (2001) refer to it as Y. We take its value to be 0.045 from the Berner and Kothavala (2001) caption to Fig. 3, "from cold periods" e.g. the last 40 Myr.

The effect of regolith erosion is to amplify the rate of silicate weathering in the region where bedrock is exposed. However, since the global rate of weathering is subject to regulation by the silicate weathering thermostat, an increase in the weatherability of the shield location will eventually act to draw down CO_2 somewhat, diminishing the rate of weathering everywhere. The model-domain mean weathering rate in the model is based on present-day data, and implicitly assumes present-day CO_2 concentration. The geochemical carbon cycle model requires that weathering rates must eventually be controlled by negative feedback with atmospheric CO_2 concentration, or else the model blows up and produces impossible atmospheric CO_2 concentrations.

A source of significant uncertainty, on which the model results depend rather sensitively, is the relative impact of Canadian Shield weathering on the global weathering budget. The model domain encompasses 27% of the land surface excluding Antarctica. However, weathering rates are extremely variable around the world, with rates in volcanic provinces, for example, exceeding those in granitic terrains by up to a factor of 100 (Millot et al., 2002), so simply scaling weathering contributions by area is too simple an approach.

The baseline, old-soil (defined as 100-kyr surface age) rate of weathering CO_2 uptake predicted by the model for the Canadian Shield is 2.7 mmol m^{-2} year. For comparison, the global average rate of CO_2 uptake, obtained by dividing the CO_2 degassing flux by the area of the earth, is 46 mmol m^{-2} yr^{-1}. The model thus predicts that in the old-soil limit, the Canadian Shield region would account for about 1.5% of global weathering. Modern observations of Canadian Shield weathering rate include $\sim$5 mmol m^{-2} yr^{-1} from the Slave province and $\sim$20 mmol m^{-2} yr^{-1} in the Grenville province (Millot et al., 2002). Using an intermediate value of $\sim$10 mmol m^{-2} yr^{-1} implies that the shield today accounts for about 6% of global weathering, within a range of 3–12%.

The model finds the Canadian Shield today weathering three times faster than the old-soil limit. The model weathering rate for the Shield given its history would be about 8 mmol m^{-2} yr^{-1}, within the range of observed weathering. We calculate a global weathering rate acceleration factor, F_{total} as

$$F_{total} = \frac{W_{model}}{W_{baseline}} A + (1 - A),$$

where W_{model} is a weathering rate from Fig. 16a (red curve). The first term on the right-hand side is the rate of weathering in the Canadian shield area, which at present equals about 6% of global weathering. $W_{baseline}$ is a baseline weathering rate, and A is a weighting factor based on the relative contribution of the Canadian shield to global weathering rates. If we choose a $W_{baseline}$ equal to the model weathering rate averaged over the glacial cycles, about 5 mmol/m^2 yr, then we require a weighting factor A of about 4% in order to fit the present-day data correctly. We bracket this best guess with additional model runs where A is taken to be 0% and 8%.

8.1.2. Carbonate weathering

The rate of carbonate weathering is also scaled according to $F_{BT}(CO_2)$, but we have omitted any sensitivity to regolith exposure or land surface area. We presume carbonate weathering to be relatively insensitive to these things because river waters in areas of carbonate bedrock and till are typically close to saturation with CaCO$_3$. River water may even be supersaturated if allowed to equilibrate with atmospheric pCO$_2$, because groundwaters are saturated at high pCO$_2$ due to soil respiration. Ice sheets cover land area, preventing weathering, but they also expose the continental shelf by lowering sea level. Detailed calculations of the effect of ice sheets on carbonate weathering (Munhoven and Francois, 1993) show enough uncertainty that constant carbonate weathering seems to be

as reasonable an assumption as any. The Holocene rate of carbonate weathering is about 10.2×10^{12} mol yr^{-1}, which combines with a silicate weathering flux of about 6.2×10^{12} mol yr^{-1} to deliver 16.5×10^{12} mol yr^{-1} of dissolved $CaCO_3$ to the ocean.

8.1.3. Coral deposition

The rate of coral reef deposition is taken from Kleypas (1997), based primarily on a table of the habitable area for coral deposition as a function of sea level, from their Table 4. For the most part, the model simply scales the deposition rate according to habitable area, between end-members of present day, with a deposition rate of 10.7×10^{12} mol yr^{-1}, and LGM, with 2.6×10^{12} mol yr^{-1}. Milliman (1993) estimated 15×10^{12} mol yr^{-1}. It is possible that the near-surface hypsometry of the ocean actually responds to sea level, by building beaches or deltas, but this is not accounted for in the model. If the rate of sea-level rise exceeds 10 m kyr^{-1}, corals begin to drown, cutting their area-specific accumulation rate by up to 50%, but in our results this does not occur often.

8.1.4. Deep sea $CaCO_3$ deposition

Deposition of $CaCO_3$ in the deep sea is taken from Archer et al. (1998), who presented model-calculated $CaCO_3$ deposition in the deep-ocean, under a frozen circulation field as a function of deep Pacific CO_3^{2-} concentration and the inventory of erodable $CaCO_3$ in surface sediments (their Fig. 16). The inventory of $CaCO_3$ affects $CaCO_3$ burial during a time of net dissolution; when $CaCO_3$ becomes depleted, dissolution slows down. Here we have neglected the effects of the amount of erodable $CaCO_3$ on $CaCO_3$ burial, and reduce the dependence to linearly on ocean CO_3^{2-} concentration. We used a rate constant of 0.25×10^{12} mol yr^{-1} per umol kg^{-1} of CO_3^{2-}. The deep sea burial of $CaCO_3$ through the model Holocene under conditions similar to the present-day is $10–15 \times 10^{12}$ mol yr^{-1}, compared with about 12 in the Hamburg model (Archer and Maier-Reimer, 1994), and estimated to be 17 by Milliman (1993).

8.1.5. Atmosphere–ocean equilibrium

Our carbon cycle model for the ocean does not consider the biological pump or the effects of circulation and heterogeneous ocean temperature (the solubility pump). The temperature is $4 °C$ at 280 ppm pCO_2, and has a climate sensitivity of $3 °C$ (Archer et al., 2004; Martin et al., 2005). The temperature of the ocean relaxes to its equilibrium temperature on a time scale of 1000 years. The rate of gas evasion is taken linearly with the pCO_2 difference between the atmosphere and the ocean, with time constant of equilibration of 300 years. The biological and solubility pumps in the ocean might seem like first-order omissions, but we believe that on long-enough time scales they can be neglected. The silicate thermostat acts to control the pCO_2 of the atmosphere, while $CaCO_3$ compensation controls the CO_3^{2-} concentration of the

ocean. The effect of a pump is to introduce an offset in the relationship between atmospheric CO_2 and ocean CO_3^{2-}. The same combination of atmospheric pCO_2 and ocean CO_3^{2-} will be achieved with or without the biological pump, because the respective thermostats demand it, but the ocean concentrations of alkalinity and total CO_2 will differ between the two cases. The GEOCARB models (Berner, 2004; Berner and Kothavala 2001) take a similar approach, but they also assume continuous equilibrium of $CaCO_3$ compensation and atmosphere ocean gas exchange. By resolving these century and millennial timescale processes, our new model is better able to address questions of weathering on glacial cycle timescales.

8.1.6. Terrestrial biosphere carbon uptake

The amount of carbon in the terrestrial biosphere changes by 500 Gton C between glacial and interglacial time. We apply a carbon flux to account for this, scaling the size of the terrestrial biosphere linearly with sea level.

8.1.7. Results

The evolution of the model through its entire 3-million year trajectory is shown in Fig. 19. The rate of silicate weathering follows the rate of CO_2 degassing, with some variability on time scales shorter than about 400 kyr. The rate of $CaCO_3$ deposition in the ocean follows the total rate of weathering on land, via the $CaCO_3$ compensation feedback in the ocean, which has a time scale of 5–10 kyr. The absolute values of atmospheric CO_2 and weathering rates are sensitive to model parameters, and are probably less meaningful than are relative changes in these values.

Ice sheets have two impacts on the rate of weathering. They denude the regolith, which increases the rate of weathering. But they also cover ground, precluding much weathering underneath. For the standard run ($A = 4\%$, black line in Fig. 19), the net effect is to make the surface of the earth more weatherable in the most recent 1.5 million years of the model run, thus bringing down atmospheric CO_2 (averaged over the intervals marked on Fig. 19) by about 7 ppm. If we neglect the enhanced weathering of the Canadian Shield ($A = 0$, blue line), we see an overall decrease of pCO_2 throughout the model run. In the initial half of the runs, weathering is inhibited by ice-sheet coverage more on average than it is enhanced by regolith exposure; hence the stronger drawdown of CO_2 where there is no impact of the ice sheets on weathering ($A = 0\%$). The balance between inhibition and amplification of weathering is difficult to constrain and not very meaningful in the model results, but the change in pCO_2 through the MPT is probably more significant. Neglecting the weathering cycles, the CO_2 drawdown through the MPT is only about 1 ppm. For the large weathering cycles ($A = 8\%$), the drawdown at the MPT is 12 ppm. Thus the model results support the proposal that enhanced weathering of the exposed Canadian Shield might have provided some climatic feedback across the MPT.
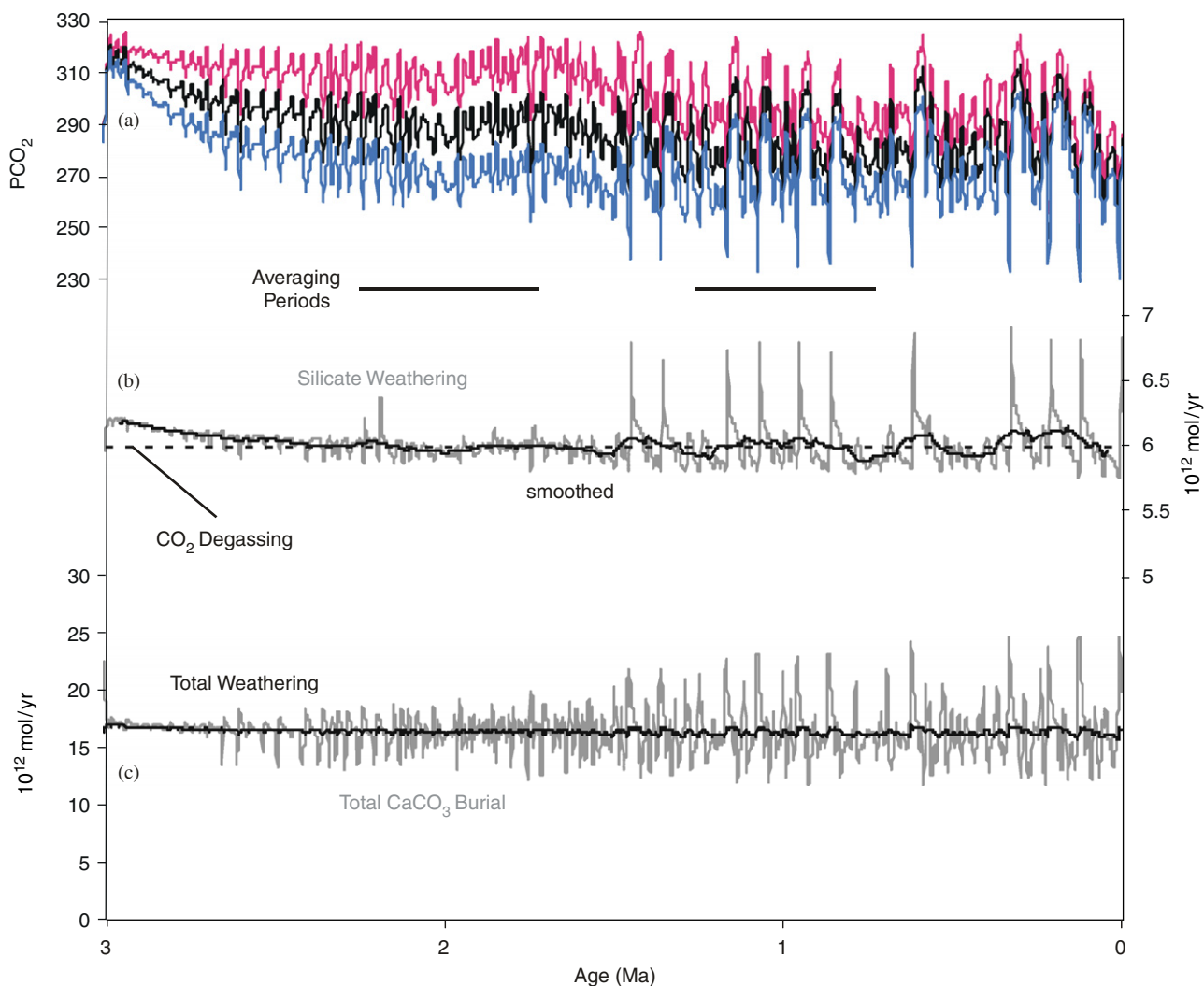
Fig. 19. Carbon cycle model results on 3 Myr timescale. (a) Atmospheric pCO2. Blue is no weathering cycles, black is the best fit to present-day weathering fluxes (4% weighting factor, and red is 8%, (b) Silicate weathering rate (grey), smoothed (black), and CO2 degassing rate (dashed), (c) Total calcium fluxes to the ocean (grey), and ocean CaCO3 burial (black).

The behavior of the model through the most recent 100-kyr ice age cycles is shown in Fig. 20. The model sea level is shown at the top, with the familiar sawtooth pattern. The pCO_2 of the atmosphere cycles by about 60 ppm over the glacial/interglacial cycles, largely because of the modulation of shallow-water $CaCO_3$ deposition (the coral reef hypothesis: Berger, 1982). This is not a realistic explanation for all of the variability of the ice-core CO_2 record, in that the timing of the CO_2 rise is too slow during terminations. Weathering rates, determined from model pCO_2 values, will not be realistic in detail for this reason, but we chose to maintain internal model consistency rather than drive weathering using observed CO_2 fluctuations. During deglaciations, the global rate of silicate weathering spikes upward by 15%, from a minimum rate of 6×10^{12} mol yr^{-1}, up to maxima of 7 or 8×10^{12} mol yr^{-1}. If we neglect the enhanced weathering of the Canadian Shield, there is a slight decrease in weathering during the deglaciation driven

by a short, sharp deglacial drawdown in the model pCO_2 value.

Carbonate weathering is affected by hydrology driven by atmospheric CO_2, but is not enhanced by the exposure of the Canadian Shield. Shallow-water $CaCO_3$ deposition in the model is not affected by the $CaCO_3$ saturation state in the ocean or temperature, just sea level. Therefore the shallow-water deposition curves are the same for all runs. The deep sea burial rate of $CaCO_3$ is a slave to the imbalance between total weathering and shallow-water deposition. In all cases there is a greater variability in the deep-ocean $CaCO_3$ deposition rate than is observed: nearly a factor of two difference between minimum and maximum values, which would have been obvious in the $CaCO_3$ distribution on the sea floor (Catubig et al., 1998). Either the cycles in shallow water $CaCO_3$ deposition are too intense in the model, or else some other process acted to mask this effect in the real carbon cycle. If the enhanced
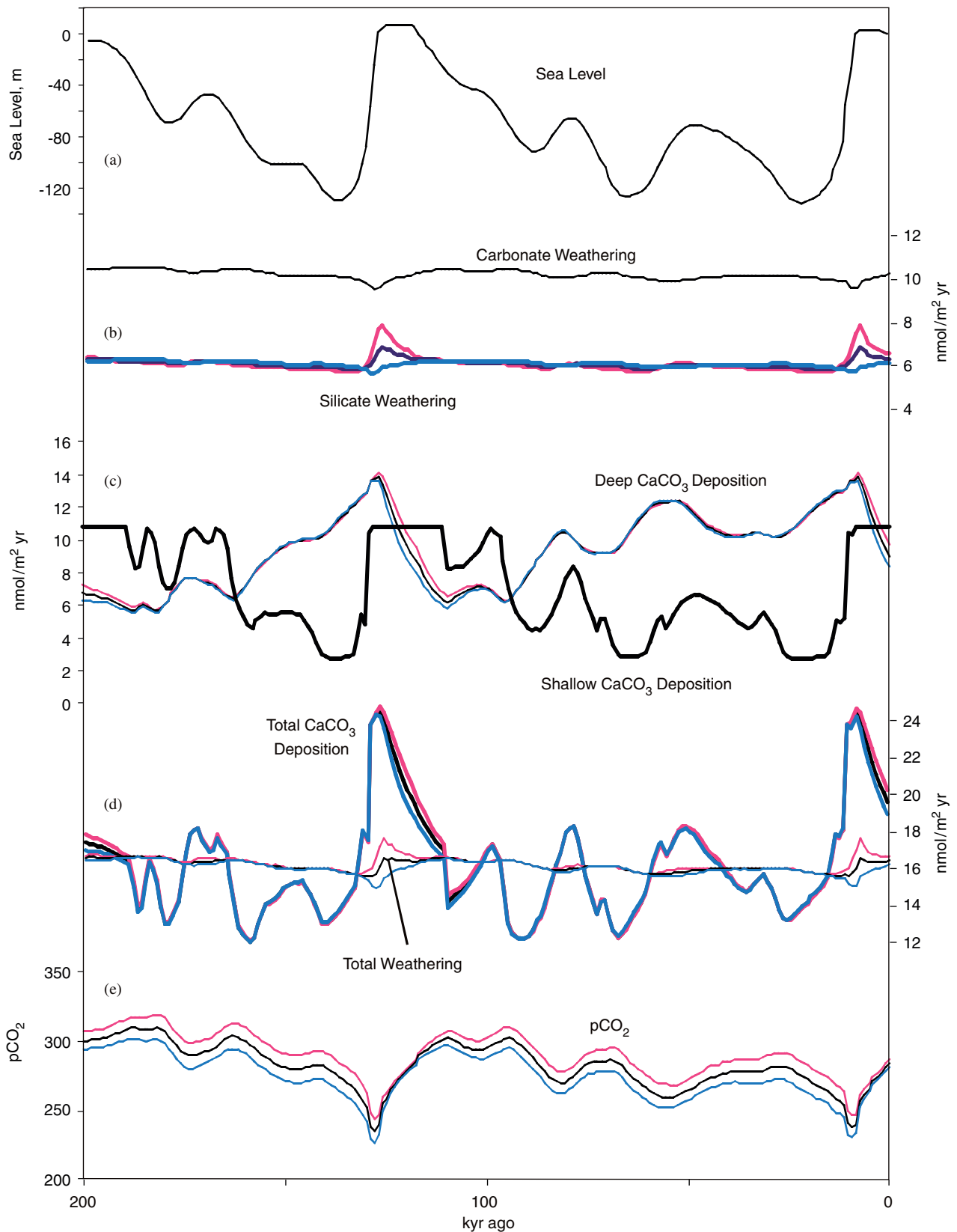
Fig. 20. Carbon cycle model results on 200-kyr timescale. Blue is no weathering cycles, black is the best fit to present-day weathering fluxes (4% weighting factor), and red is 8%. (a) Sea level, (b) Weathering rates, carbonate and silicate, (c) Shallow (heavy line) and deep (thin lines) $CaCO_3$ deposition in the ocean, (d) Total ocean $CaCO_3$ burial rate, sum of the terms in (**c**) (heavy lines), and total weathering, the total of the terms in (b) (thin lines), (e) pCO_2 of the atmosphere.

weathering cycles in the Canadian Shield were larger, they could help solve the problem by supplying alkalinity to the ocean just as the coral reefs demand it. Our best result from the model, however, is that the cycles of alkalinity fluxes from the shield exposure are too small to balance our estimate of the coral reef effect.

8.1.8. Carbon cycle summary

Glacial erosion of the accumulated soils on the Canadian Shield can explain a long-term pCO_2 drawdown of about 7–12 ppm, enough perhaps to act as a feedback in causing the MPT. Over glacial/interglacial cycles, the shield-weathering cycle acts as a stabilizing effect on atmospheric CO_2, drawing CO_2 down during the interglacial times when it is observed to be highest. The glacial pCO_2 problem is not solved, but perhaps the shield-weathering cycles could explain the alkalinity source for coral reef growth during high stands, if it were a larger effect than the model predicts it to be.

9. Conclusions

Among the most intriguing issues first brought to light by Shackleton's pioneering research concerns the question of the emergence of the 100-kyr ice-volume cycle during the middle Pleistocene in the absence of any change in the orbital forcing. There is wide disagreement in defining when this MPT occurred, with descriptions ranging from an abrupt versus gradual transition that began as early as 1500 ka and as late as 600 ka (e.g., Pisias and Moore, 1981; Prell, 1982; Ruddiman et al., 1989; Park and Maasch, 1993; Mudelsee and Schulz, 1997; Rutherford and D'Hondt, 2000). To a large extent, these differing conclusions can be explained by the analysis of individual $\delta^{18}O_b$ records, the details of which may differ due to regional differences in salinity and temperature, masking the global ice-volume and deep-water temperature signal. Our analysis of the recently constructed LR04 "stacked" $\delta^{18}O_b$ record (Lisiecki and Raymo, 2005) that best represents a global signal indicates that the MPT began 1250 ka with a gradual increase (decrease) in average ice volume (deep-water temperature), accompanied by an increase in the amplitude of the variability, with this transition reaching completion by 700 ka. Analysis of the frequency domain, however, suggests that while the emergence of the low-frequency signal also began 1250 ka, that signal disappeared for ~100 kyr before reemerging as a persistent signal since 900 ka. In summary, these results suggest that the MPT was characterized by an increase in the severity of glaciations that paralleled the emergence of the ~100-kyr cycle starting at 1250 ka, with maximum glaciations being established at the same time (700 ka) as the establishment of the dominant 100-kyr cycles.

There are currently few data available to constrain how much of the increase in amplitude of the $\delta^{18}O_b$ cycles represents an increase in ice volume relative to additional global cooling of deep-water during glaciations. Dwyer et al. (1995) concluded that the $\delta^{18}O_{SW}$ signal in their North Atlantic benthic ostracodes record was ~0.4 per mil lower in the late Pliocene relative to the late Pleistocene. Application of the $\delta^{18}O_{SW}$/sea level relation (0.008 per mil m^{-1}) to the ~0.4 per mil increase in $\delta^{18}O_{SW}$ thus suggests that post-MPT ice sheets were ~50 m larger, in sea-level equivalent, than pre-MPT ice sheets. Using the constraints imposed by the Dwyer et al. (1995) data on changes in $\delta^{18}O_{SW}$, we then estimate a decrease in global deep-water temperature recorded by the LR04 stack of ~1.2 °C during 100-kyr glaciations relative to 41-kyr glaciations.

Changes in other components of the climate system indicate differing sensitivities to the changes in global ice volume and deep-water temperature that occurred during the MPT. The onset of the MPT was accompanied by decreases in sea surface temperatures (SSTs) in the North Atlantic (Ruddiman et al., 1989) and tropical-ocean upwelling regions (Schefus et al., 2004; Liu and Herbert, 2004; McClymont and Rossel-Mele, 2005) and by an increase in African (Tiedemann et al., 1994) and Asian aridity and monsoonal intensity (Clemens et al., 1996; Williams et al., 1997; Sun et al., 2006). The low-frequency component of North Atlantic SSTs and proxies of Asian and African monsoon and aridity also appeared at this time. Finally, glacial $\delta^{13}C$ values of NADW and CDW become more depleted at the start of the MPT, and both a significant change in ocean circulation and a transient transfer of carbon from the organic to inorganic pools is likely.

Additional changes at 900 ka indicate this to be an important time during the MPT, beginning with an 80-kyr event of extreme SST cooling and reduction in deep-ocean circulation followed by the partial recovery and subsequent stabilization of long-term North Atlantic and tropical ocean SSTs, increasing Southern Ocean SST variability primarily associated with warmer interglacials, the loss of permanent subpolar sea-ice cover, and the emergence of low-frequency variability in Pacific SSTs and global deep-ocean circulation.

Since 900 ka, ice sheets have been the only component of the climate system to exhibit persistent low-frequency variability. With the exception of a near-universal organization of low-frequency power associated with marine isotope stages 11 and 12, the spectrograms of all other components suggest a complex picture of the relationship between climate response to astronomical and ice-sheet forcing. The spectrograms do not show single, persistent frequency components, but rather an inconsistent distribution of power in frequency–time space. This is likely the result of at least two important circumstances: the low-frequency forcing is quasi-periodic, in the sense that it is composed of more than six independent periods in the interval from 66 to 200 kyr, with estimated values that vary with age (Berger et al., 2005). The second reason has to do with the fact that the response of the climate system to the low-frequency astronomical forcing is nonlinear, which

causes the dependence of the response's frequencies and phases to the insolation's frequencies and phases to be distinctly different from the simplistic view that insolation drives or paces climate change directly and proportionately. The spectrograms do suggest that the climate system might behave as a slightly forced, highly nonlinear system. If so, the result should be a climate system that goes through periods of 'capture' and 'escape' from the forcing. The system seems to jump from one state to the other at random times when excited by the low-frequency forcing. We speculate, however, that the process is actually governed by deterministic, yet chaotic, laws, with the randomness being a consequence of complicated nonlinearity. Rial et al. (submitted) illustrated an example of such a mechanism by showing that a simple, but nonlinear, differential equation representing the climate's response forced by the Milankovitch insolation closely reproduces the apparently random sequence of Dansgaard-Oescher pulses of the last 100 kyr recorded in the GRIP ice core.

The emergence of low-frequency, high-amplitude, quasi-periodic (~100-kyr) glacial variability during the middle Pleistocene in the absence of any change in orbital forcing indicates a fundamental change internal to the climate system. Most hypotheses for the origin of the MPT invoke a response to a long-term cooling, possibly induced by decreasing atmospheric pCO_2 (Raymo, 1997; Paillard, 1998; Berger et al., 1999; Tziperman and Gildor 2003). None of these hypotheses, however, accounts for the geological constraint that the earliest Northern Hemisphere ice-sheets covered a similar or larger area than those that followed the MPT (Boellstorf, 1978; Roy et al., 2004a; Balco et al., 2005). Given that the MPT was associated with an increase in ice volume, this constraint requires that post-MPT ice sheets were substantially thicker than pre-MPT ice sheets, indicating a change in subglacial conditions that influence ice dynamics. Clark and Pollard (1998) proposed that such an increase in ice thickness occurred as crystalline Precambrian Shield bedrock became exposed by glacial erosion of a thick mantle of regolith. This exposure of a high-friction substrate caused thicker ice sheets, with an attendant change in their response to the orbital forcing.

Modeling indicates that regolith erosion and resulting exposure of crystalline bedrock would cause an increase in long-term silicate weathering rates, in good agreement with marine Sr and Os isotopic records. A carbon cycle model that accounts for an increase in silicate weathering indicates that atmospheric pCO_2 would decrease by 7–12 ppm, suggesting that the attendant cooling may have been an important feedback to the changes in subglacial processes that caused the MPT in the Clark and Pollard (1998) model.

Acknowledgments

References

Andrews, J.T., 1993. Changes in the silt- and clay-size mineralogy of sediments at Ocean Drilling Program Site 645B. Baffin Bay: Canadian Journal of Earth Sciences 30, 2448–2452.

Archer, D.E., Maier-Reimer, E., 1994. Effect of deep-sea sedimentary calcite preservation on atmospheric CO_2 concentration. Nature 367, 260–264.

Archer, D., Kheshgi, H., Maier-Reimer, E., 1998. Dynamics of fossil fuel CO_2 neutralization by marine $CaCO_3$. Global Biogeochemical Cycles 12, 259–276.

Archer, D., Martin, P., Buffett, B., Brovkin, V., Rahmstorf, S., Ganopolski, A., 2004. The importance of ocean temperature to global biogeochemistry. Earth and Planetary Science Letters 222, 333–348.

Armstrong, R.L., 1971. Glacial erosion and the variable isotopic composition of strontium in seawater. Nature 230, 132–133.

Balco, G., Rovey, C.W., Stone, J.O.H., 2005. The first glacial maximum in North America. Science 307, 222.

Becquey, S., Gersonde, R., 2002. Past hydrographic and climatic changes in the Subantarctic Zone of the South Atlantic: the Pleistocene record from ODP Site 1090. Palaeogeography, Palaeoclimatology, Palaeoecology 182, 221–239.

Berger, A., Li, X.S., Loutre, M.F., 1999. Modeling northern hemisphere ice volume over the last 3 Ma. Quaternary Science Reviews 18, 1–11.

Berger, A., Melice, J.L., Loutre, M.F., 2005. On the origin of the 100-kyr cycles in the astronomical forcing. Paleoceanography 20, PA4019.

Berger, W.H., 1982. Increase of carbon dioxide in the atmosphere during deglaciation: the coral reef hypothesis. Naturwissenshaften 69, 87–88.

Berner, R.A., 2004. The Phanerozoic Carbon Cycle: CO_2 and O_2. Oxford University Press, Oxford, 150pp.

Berner, R.A., Kothavala, Z., 2001. GEOCARB III: a revised model of atmospheric CO_2 over Phanerozoic time. American Journal of Science 301, 182–204.

Blum, J.D., 1997. The effect of late Cenozoic glaciation and tectonic uplift on silicate weathering rates and the marine $^{87}Sr/^{86}Sr$ record. In: Ruddiman, W.F. (Ed.), Tectonic Uplift and Climate Change. Plenum Press, New York, pp. 259–288.

Blum, J.D., Erel, Y., 1995. A silicate weathering mechanism linking increases in marine $^{87}Sr/^{86}Sr$ with global glaciation. Nature 373, 415–418.

Boellstorf, J., 1978. North American Pleistocene stages reconsidered in the light of probable Pliocene–Pleistocene continental glaciation. Science 202, 305–307.

Boulton, G.S., Hindmarsh, R.C.A., 1987. Sediment deformation beneath glaciers: rheology and geological consequences. Journal of Geophysical Research 92, 9059–9082.

Boyle, E.A., Keigwin, L.D., 1987. North Atlantic thermohaline circulation during the last 20,000 years linked to high latitude surface temperature. Nature 330, 35–40.

Broecker, W.S., 1982. Glacial to interglacial changes in ocean chemistry. Progress in Oceanography 11, 151–197.

Broecker, W.A., Maier-Reimer, E., 1992. The influence of air and sea exchange on the carbon isotope distribution in the sea. Global Biogeochemical Cycles 6, 315–320.

Burton, K.W., Bourdon, B., Birck, J.-L., Allegre, C.J., Hein, J.R., 1999. Osmium isotope variations in the oceans recorded by Fe–Mn crusts. Earth and Planetary Science Letters 171, 185–197.

Capo, R.C., DePaolo, D.J., 1990. Seawater strontium isotopic variations from 2.5 million years ago to present. Science 249, 51–55.

Catubig, N.R., Archer, D.E., Francois, R., deMenocal, P.B., Howard, W., Yu, E.-F., 1998. Global deep-sea burial rate of calcium carbonate during the Last Glacial Maximum. Paleoceanography 13, 298–310.

Clark, P.U., Pollard, D., 1998. Origin of the Middle Pleistocene transition by ice sheet erosion of regolith. Paleoceanography 13, 1–9.

Clark, P.U., Alley, R.B., Pollard, D., 1999. Northern Hemisphere ice-sheet influences on global climate change. Science 286, 1104–1111.

Clark, P.U., Mix, A.C., 2000. Ice sheets by volume. Nature 406, 689–690.

Clarke, G.K.C., Marshall, S.J., 2002. Isotopic balance of the Greenland Ice Sheet: modelled concentrations of water isotopes from 30,000 BP to present. Quaternary Science Reviews 21, 419–430.

Clemens, S.C., Murray, D.W., Prell, W.L., 1996. Non-stationary phase of the Plio-Pleistocene Asian monsoon. Science 274, 943–948.

Crowley, T.J., 1992. North Atlantic Deep Water cools the Southern Hemisphere. Paleoceanography 7, 489–497.

Cuffey, K.M., Alley, R.B., 1996. Is erosion by deforming subglacial sediments significant? (towards till continuity). Annals of Glaciology 22, 17–24.

De Garidel-Thoron, T., Rosenthal, Y., Bassinot, F., Beaufort, L., 2005. Stable sea surface temperatures in the western Pacific warm pool over the past 1.75 million years. Nature 433, 294–298.

deMenocal, P.B., 1995. Plio-Pleistocene African climate. Science 270, 53–59.

Derry, L.A., France-Lanord, C., 1996. Neogene Himalayan weathering history and river $^{87}Sr/^{86}Sr$: impact on the marine Sr record. Earth and Planetary Science Letters 142, 59–74.

Duplessy, J.-C., Shackleton, N.J., Fairbanks, R.G., Labeyrie, L., Oppo, D., Kallel, N., 1988. Deepwater source variations during the last climatic cycle and their impact on the global deepwater circulation. Paleoceanography 3, 343–360.

Dwyer, G.S., Cronin, T.M., Baker, P.A., Raymo, M.E., Buzas, J.S., Correge, T., 1995. North Atlantic deepwater temperature change during late Pliocene and late Quaternary climatic cycles. Science 270, 1347–1351.

Emiliani, C., 1955. Pleistocene temperatures. Journal of Geology 63, 538–578.

Farrell, J.W., Prell, W.L., 1991. Pacific $CaCO_3$ preservation and $\delta^{18}O$ since 4 Ma: paleoceanographic and paleoclimatic implications. Paleoceanography 6, 485–498.

Farrell, J.W., Clemens, S.C., Gromet, L., 1995. Improved chronostratigraphic reference curve of late Neogene seawater $^{87}Sr/^{86}Sr$. Geology 23, 403–406.

Goldich, S.S., 1938. A study in rock weathering. Journal of Geology 46, 17–58.

Hays, J.D., Imbrie, J., Shackleton, N.J., 1976. Variations in the Earth's orbit: pacemaker of the ice ages. Science 194, 1121–1132.

Hodell, D.A., Mueller, P.A., McKenzie, J.A., Mead, G.A., 1989. Strontium isotope stratigraphy and geochemistry of the late Neogene ocean. Earth and Planetary Science Letters 92, 165–178.

Hodell, D.A., Venz, K.A., Charles, C.D., Ninneman, U.S., 2003. Pleistocene vertical carbon isotope and carbonate gradients in the South Atlantic sector of the Southern Ocean. Geochemistry, Geophysics, Geosystems 4, 1004.

Huybers, P., Wunsch, C., 2004. A depth-derived Pleistocene age-model: uncertainty estimates, sedimentation variability, and nonlinear climate change. Paleoceanography 19.

Huybers, P., Wunsch, C., 2005. Obliquity pacing of the late Pleistocene glacial terminations. Nature 434, 491–494.

Imbrie, J., Imbrie, J.Z., 1980. Modeling the climatic response to orbital variations. Science 207, 943–953.

Imbrie, J., Hays, J.D., Martinson, D.G., McIntyre, A., Mix, A.C., Morley, J.J., Pisias, N.G., Prell, W.L., Shackleton, N.J., 1984. The orbital theory of Pleistocene climate: support from a revised chronology of the marine $\delta^{18}O$ record. In: Berger, A., et al. (Eds.), Milankovitch and Climate, Part 1. D. Reidel, Norwell, MA, pp. 269–305.

Jansen, E., Fronval, T., Rack, F., Channell, J.E.T., 2000. Pliocene–Pleistocene ice rafting history and cyclicity in the Nordic Seas during the last 3.5 Myr. Paleoceanography 15, 709–721.

Jenson, J.W., MacAyeal, D.R., Clark, P.U., Ho, C.L., Vela, J.C., 1996. Numerical modeling of subglacial sediment deformation: implications for the behavior of the Lake Michigan Lobe, Laurentide ice sheet. Journal of Geophysical Research 101, 8717–8728.

Joyce, J.E., Tjalsma, L.R.C., Prutzman, J.M., 1993. North American glacial meltwater history for the past 2.3 My, oxygen isotope evidence from the Gulf of Mexico. Geology 21, 483–486.

Kennett, J.P., Shackleton, N.J., 1975. Laurentide ice sheet meltwater recorded in 'Gulf' of Mexico deep-sea cores. Science 188, 147–150.

Kitamura, A., Kawagoe, T., 2006. Eustatic sea-level change at the Mid-Pleistocene climate transition: new evidence from the shallow-marine sediment record of Japan. Quaternary Science Reviews 25, 323–335.

Kleypas, J.A., 1997. Modeled estimates of global reef habitat and carbonate production since the last glacial maximum. Paleoceanography 12, 533–545.

Laskar, J., Joutel, F., Boudin, F., 1993. Orbital, precessional, and insolation quantities for the Earth from -20 Myr to $+10$ Myr. Astronomy and Astrophysics 270, 522–533.

Lea, D.W., Martin, P.A., Pak, D.K., Spero, H.J., 2002. Reconstructing a 350 ky history of sea level using planktonic Mg/Ca and oxygen isotope records from a Cocos Ridge core. Quaternary Science Reviews 21, 283–293.

Lisiecki, L.E., Raymo, M.E., 2005. A Pliocene–Pleistocene stack of 57 globally distributed benthic $\delta^{18}O$ records. Paleoceanography 20, PA1003.

Liu, Z., Herbert, T.D., 2004. High-latitude influence on the eastern equatorial Pacific climate in the early Pleistocene epoch. Nature 427, 720–723.

Marlow, J.R., Lange, C.B., Wefer, G., Rosell-Mele, A., 2000. Upwelling intensification as part of the Pliocene–Pleistocene climate transition. Science 290, 2288–2291.

Marshall, S.J., Clark, P.U., 2002. Basal temperature evolution of North American ice sheets and implications for the 100-kyr cycle. Geophysical Research Letters 29 (24), 2214.

Martin, P., Archer, D., Lea, D., 2005. Role of deep sea temperatures in the carbon cycle during the Last Glacial. Paleoceanography 20, PA2015.

Martin, P.A., Lea, D.W., Rosenthal, Y., Shackleton, N.J., Sarnthein, M., Papenfuss, T., 2002. Quarternary deep sea temperature histories derived from benthic foraminiferal Mg/Ca. Earth and Planetary Science Letters 198 (1–2), 193–209.

McClymont, E.L., Rossel-Mele, A., 2005. Links between the onset of modern Walker circulation and the mid-Pleistocene climate transition. Geology 33, 389–392.

McKeague, J.A., Grant, D.R., Kodama, H., Beke, G.J., Wang, C., 1983. Properties of a soil and the underlying gibbsite-bearing saprolite, Capre Breton Island, Canada. Canadian Journal of Earth Sciences 20, 37–48.

McManus, J.F., Francois, R., Gherardi, J.-M., Keigwin, L.D., Brown-Leger, S., 2004. Collapse and rapid resumption of Atlantic meridional circulation linked to deglacial climate changes. Nature 428, 834–837.

Medina-Elizalde, M., Lea, D.W., 2005. The mid-Pleistocene transition in the tropical Pacific. Science 310, 1009–1012.

Milliman, J.D., 1993. Production and accumulation of calcium carbonate in the ocean: budget of a non-steady state. Global Biogeochemical Cycles 7, 927–957.

Millot, R., Gaillardet, J., Dupre, B., Allegre, C.J., 2002. The global control of silicate weathering rates and the coupling with physical erosion: new insights from rivers of the Canadian Shield. Earth and Planetary Science Letters 196, 83–98.

Mills, H.H., Delcourt, P.A., 1991. Quaternary geology of the Appalachian Highlands and interior low plateaus. In: Morrison, R.B. (Ed.), The Geology of North America, v. K2, Quaternary Nonglacial Geology: Conterminous USA. Geological Society of America, pp. 611–628.

Mix, A.C., Ruddiman, W.F., 1984. Oxygen isotope analyses and Pleistocene ice volumes. Quaternary Research 21, 1–20.

Mix, A.C., Ruddiman, W.F., McIntyre, A., 1986. Late Quaternary paleoceanography of the tropical Atlantic, I: spatial variability of annual mean sea-surface temperatures, 0–20,000 years B.P. Paleocean-ography 1, 43–66.

Mix, A.C., Le, J., Shackleton, N.J., 1995a. Benthic foraminifer stable isotope stratigraphy of Site 846: 0–1.8 Ma. In: Pisias, N.G., Mayer, L., Janecek, T., Palmer-Julson, A., van Andel, T.H. (Eds.), Proceedings of the ODP, Scientific Results, vol. 138. Ocean Drilling Program, College Station, TX, pp. 839–856.

Mix, A.C., Pisias, N.G., Rugh, W., Wilson, J., Morey, A., Hagelberg, T.K., 1995b. Benthic foraminifer stable isotope record from Site 849 (0–5 Ma): Local and global climate changes: In: Pisias, N.G., Mayer, L.A., Janecek, T.R., Palmer-Julson, A., van Andel, T.H., (Eds.), Proceedings of the Ocean Drilling Program. Scientific Results, vol. 138, pp. 371–412.

Mudelsee, M., Schulz, M., 1997. The Mid-Pleistocene climate transition: onset of 100 ka cycle lags ice volume build-up by 280 ka. Earth and Planetary Science Letters 151, 117–123.

Munhoven, G., Francois, L.M., 1993. Glacial–interglacial changes in continental weathering: possible implications for atmospheric CO_2. In: Zahn, R. (Ed.), Carbon Cycling in the Glacial Ocean: Constraints on the Ocean's Role in Global Change. Springer, Berlin.

Oerlemans, J., 1984. On the origin of the ice ages. In: Berger, A.L., et al. (Eds.), Milankovitch and Climate, Part 2. D. Reidel, Norwell, MA, pp. 607–611.

Paillard, D., 1998. The timing of Pleistocene glaciations from a simple multiple-state climate model. Nature 391, 378–381.

Park, J., Maasch, K., 1993. Plio-Pleistocene time evolution of the 100-kyr cycle in marine paleoclimate records. Journal of Geophysical Research 98, 447–462.

Paterson, W.S.B., 1972. Laurentide Ice Sheet: estimated volumes during late Wisconsin. Reviews of Geophysics and Space Physics 10, 885–917.

Peucker-Ehrenbrink, B., Blum, J., 1999. Re–Os isotope systematics and weathering of Precambrian crustal rocks: implications for the marine osmium isotope record. Geochimica et Cosmochimica Acta 62, 3193–3203.

Pikovsky, A., Rosenblum, M., Kurths, J., 2001. Synchronization. Cambridge University Press, Cambridge, UK.

Pisias, N.G., Moore Jr., T.C., 1981. The evolution of the Pleistocene climate: a time series approach. Earth and Planetary Science Letters 52, 450–458.

Prell, W.L., 1982. Oxygen and carbon isotope stratigraphy for the Quaternary of hole 502B: evidence for two modes of isotopic variability. Initial Reports DSDP 68, 455–464.

Prell, W.L., Imbrie, J., Martinson, D.G., Morley, J.J., Pisias, N.G., Shackleton, N.J., Streeter, H.F., 1986. Graphic correlation of oxygen isotope stratigraphy: application to the Late Quaternary. Paleocean-ography 1, 137–162.

Raymo, M.E., 1997. The timing of major climate transitions. Paleocean-ography 12, 577–585.

Raymo, M.E., Ruddiman, W.F., Froelich, P.N., 1988. Influence of late Cenozoic mountain building on ocean geochemical cycles. Geology 16, 649–653.

Raymo, M.E., Ruddiman, W.F., Shackleton, N.J., Oppo, D.W., 1990. Evolution of Atlantic–Pacific $\delta^{13}C$ gradients over the last 2.5 m.y. Earth and Planetary Science Letters 97, 353–368.

Raymo, M.E., Oppo, D.W., Curry, W., 1997. The mid-Pleistocene climate transition: a deep sea carbon isotopic perspective. Paleoceanography 12, 546–559.

Raymo, M.E., Oppo, D.W., Flower, B.P., Hodell, D.A., McManus, J.F., Venz, K.A., Kleiven, K.F., McIntyre, K., 2004. Stability of North Atlantic water masses in face of pronounced climate variability during the Pleistocene. Paleoceanography 19, PA2008.

Rial, J.A., 1999. Pacemaking the Ice Ages by frequency modulation of Earth's orbital eccentricity. Science 285, 564–568.

Rial, J.A., 2004. Abrupt climate change: chaos and order at orbital and millennial scales. Global and Planetary Change 41, 95–109.

Rial, J.A., Yang, M., Noone, D., submitted. Is abrupt climate change predictable? Geophysical Research Letters.

Richter, F.M., Rowley, D.B., DePaolo, D.J., 1992. Sr isotope evolution of seawater: the role of tectonics. Earth Planetary Science Letters 109, 11–23.

Roy, M., Clark, P.U., Barendregt, R.W., Glassman, J.R., Enkin, R.J., Baker, J., 2004a. Glacial stratigraphy and paleomagnetism of late Cenozoic deposits of the north-central US. Geological Society of America Bulletin 116, 30–41.

Roy, M., Clark, P.U., Raisbeck, G.M., Yiou, F., 2004b. Geochemical constraints on the origin of the Middle Pleistocene Transition from the glacial sedimentary record of the north-central US. Earth and Planetary Science Letters 227, 281–296.

Ruddiman, W.F., McIntyre, A., 1981. Oceanic mechanisms for amplifica-tion of the 23,000 year ice-volume cycle. Science 212, 617–627.

Ruddiman, W., Raymo, M., Martinson, D., Clement, B., Backman, J., 1989. Pleistocene evolution: Northern Hemisphere ice sheets and North Atlantic Ocean. Paleoceanography 4, 353–412.

Rutherford, S., D'Hondt, S., 2000. Early onset and tropical forcing of 100,000-year Pleistocene glacial cycles. Nature 408, 72–75.

Saltzman, B., 1982. Stochastically driven climatic fluctuations in the sea-ice, ocean temperature, CO_2, feedback system. Tellus 34, 97–112.

Saltzman, B., Maasch, K.A., 1991. A first-order global model of late Cenozoic climatic change II: a simplification of CO_2 dynamics. Climate Dynamics 5, 201–210.

Setterholm, D.R., Morey, G.B., 1995. An extensive pre-Cretaceous weathering profile in east-central and southwestern Minnesota. US Geological Survey Bulletin 1989, p. 29.

Schefus, E., Sinninghe Damste, J.S.S., Jansen, J.H.F., 2004. Forcing of tropical Atlantic sea surface temperatures during the mid-Pleistocene transition. Paleoceanography 19, PA4029.

Schrag, D.P., Hampt, G., Murray, D.W.S., 1996. Pore fluid constraints on the temperature and oxygen isotopic composition of the glacial ocean. Science 272, 1930–1932.

Schrag, D.P., Adkins, J.F., McIntyre, K., Alexander, J.L., Hodell, D.A., Charles, C.D., McManus, J.F., 2002. The oxygen isotopic composition of seawater during the Last Glacial Maximum. Quaternary Science Reviews 21, 331–342.

Shackleton, N.J., 1967. Oxygen isotope analyses and Pleistocene temperatures re-assessed. Nature 215, 15–17.

Shackleton, N.J., 1977. Tropical rainforest history and the equatorial Pacific carbonate dissolution cycles. In: Anderson, N.R., Malahoff, A. (Eds.), Fate of Fossil Fuel CO_2 in the Oceans. Plenum, New York, pp. 401–427.

Shackleton, N.J., 2000. The 100,000-year ice-age cycle identified and found to lag temperature, carbon dioxide, and orbital eccentricity. Science 289, 1897–1902.

Shackleton, N.J., Opdyke, N.D., 1976. Oxygen-isotope and paleomagnetic stratigraphy of Pacific core V28-239: Late Pliocene to latest Pleistocene. Geological Society of America Memoir 145, 449–464.

Shackleton, N.J., Berger, A., Peltier, W.R., 1990. An alternative astronomical calibration of the lower Pleistocene timescale based on ODP Site 677. Transactions of the Royal Society of Edinburgh 81, 251–261.

Shackleton, N.J., Imbrie, J., Hall, M.A., 1983. Oxygen and carbon isotope record of East Pacific core V19-30: implications for the formation of deep water in the late Pleistocene North Atlantic. Earth and Planetary Science Letters 65, 233–244.

Siegenthaler, U., et al., 2005. Stable carbon cycle–climate relationship during the late Pleistocene. Science 310, 1313–1317.

Skinner, L.C., Shackleton, N.J., 2005. An Atlantic lead over Pacific deep-water change across Termination I: implications for the application of the marine isotope stage stratigraphy. Quaternary Science Reviews 24, 571–580.

Sun, Y., Clemens, S.C., An, Z., Yu, Z., 2006. Astronomical timescale and palaeoclimatic implication of stacked 3.6-Myr monsoon records

from the Chinese Loess Plateau. Quaternary Science Reviews 25, 33–48.

Thiebault, F., Cremer, M., Bebrabant, P., Foulon, J., Nielson, O.B., Zimmerman, H., 1989. Analysis of sedimentary facies, clay mineralogy, and geochemistry of the Neogene-Quaternary sediments in Site 645, Baffin Bay: Proceedings Ocean Drilling Program. Scientific Results 105, 83–100.

Tiedemann, R., Sarnthein, M., Shackleton, N.J., 1994. Astronomic timescale for the Pliocene Atlantic $\delta^{18}O$ and dust flux records of Ocean Drilling Program Site 659. Paleoceanography 9, 619–638.

Toggweiler, J.R., 1999. Variation of atmospheric CO_2 by ventilation of the ocean's deepest water. Paleoceanography 14, 571–588.

Tziperman, E., Gildor, H., 2003. On the mid-Pleistocene transition to 100-kyr glacial cycles and the asymmetry between glaciation and deglaciation times. Paleoceanography 18.

van der Flierdt, T., Frank, M., Lee, D., Halliday, A.N., 2002. Glacial weathering and the hafnium isotope of seawater. Earth and Planetary Science Letters 198, 167–175.

Waelbroeck, C., Labeyrie, L., Michel, E., Duplessy, J.C., McManus, J.F., Lambeck, K., Balbon, E., Labracherie, M., 2002. Sea-level and deep water temperature changes derived from benthic foraminifera isotopic records. Quaternary Science Reviews 21, 295–305.

Wang, C., Ross, G.J., Rees, H.W., 1981. Characteristics of residual and colluvial soils developed on granite and the associated pre-Wisconsin landforms in north-central New Brunswick. Canadian Journal of Earth Sciences 18, 487–494.

White, A.F., Brantley, S.L., 2003. The effect of time on the weathering of silicate minerals: why do weathering rates differ in the laboratory and field? Chemical Geology 202, 479–506.

Williams, D.F., Peck, J., Karabanov, E.B., Prokopenko, A.A., Kravchinsky, V., King, J., Kuzmin, M.I., 1997. Lake Baikal record of continental climate response to orbital insolation during the past 5 million years. Science 278, 1114–1117.

Yokoyama, Y., Lambeck, K., De Deckker, P.P.J., Fifield, L.K., 2000. Timing of the last glacial maximum from observed sea-level minima. Nature 406, 713–716.